A Shallow-Convection Parameterization for Mesoscale Models. Part I: Submodel Description and Preliminary Applications

AIJUN DENG AND NELSON L. SEAMAN

Department of Meteorology, The Pennsylvania State University, University Park, Pennsylvania

JOHN S. KAIN

National Severe Storms Laboratory, Norman, Oklahoma

(Manuscript received 12 January 2001, in final form 14 June 2002)

ABSTRACT

A shallow-convection parameterization suitable for both marine and continental regimes is developed for use in mesoscale models. The scheme is closely associated with boundary layer turbulence processes and can transition to either a deep-convection scheme in conditionally unstable environments or to an explicit (resolved scale) moisture scheme in moist stable environments. The shallow-convection mass-closure assumption uses a hybrid formulation based on boundary layer turbulent kinetic energy (TKE) and convective available potential energy (CAPE), while the convective trigger is primarily a function of boundary layer TKE. Secondary subgrid clouds having nearly neutral buoyancy can form as shallow-convective updrafts detrain mass to their environment. Called *neutrally buoyant clouds* (NBCs), these can be dissipated through lateral and vertical mixing, light precipitation, ice-crystal settling, and cloud-top entrainment instability (CTEI).

The shallow-convection scheme is developed and demonstrated in a 1D version of the fifth-generation Pennsylvania State University–National Center for Atmospheric Research (PSU–NCAR) mesoscale model (MM5) which includes a 1.5-order turbulence parameterization that predicts the TKE, an atmospheric radiation submodel, and an explicit moisture submodel. The radiation calculation includes the feedback effects of the subgrid NBCs predicted by the shallow-convection parameterization. Results from initial applications in both marine and continental environments are consistent with the observed characteristics of the mesoscale thermodynamic structures and local cloud-field parameters. A subsequent paper (Part II) presents more complete verifications in different environments and results of sensitivity experiments.

1. Introduction

Convective clouds are well known to be crucial components of weather and climate. They not only transport heat and moisture vertically in the atmosphere, but also strongly affect solar and longwave radiation budgets from local to global scales (Lilly 1968; Ackerman 1991). Because of their significance, most computer models used for climate or numerical weather prediction (NWP) include some representation of these clouds. In particular, since convective clouds have characteristic scales ($\sim 10^2$–10^3 m) that are smaller than the well-resolved scales of the aforementioned models, they generally are represented as subgrid-scale entities through a parameterization.

Historically, most numerical research involving parameterizations of convective clouds has focused on deep (precipitating) rather than shallow (mostly non-precipitating) clouds. However, shallow convection can have significant impacts on the mesoscale, as well as the larger scales. For example, by affecting the net radiation characteristics of the atmosphere, shallow convection can contribute to the development of mesoscale circulations (Wetzel et al. 1996). By modifying the thermodynamic profiles in the environment, it can affect the timing and location of deep convection initiation. Moreover, convective clouds can have strong influences on air quality by venting boundary layer pollutants to higher levels, initiating aqueous chemical reactions that lead to the formation of secondary aerosol, and by altering the actinic radiation flux (McHenry et al. 1996). Thus, realistic parameterizations of shallow convective clouds can be crucial not only in climate and weather prediction, but for air chemistry models as well.

Numerous approaches have been used to parameterize the effects of shallow convection. For example, Lilly (1968) described a mixed-layer cloud model used to simulate a stratocumulus-topped marine boundary layer. This approach has been widely used, especially in general circulation models. However, the well-mixed assumption limits its ability to represent the complexity

Corresponding author address: Aijun Deng, Dept. of Meteorology, The Pennsylvania State University, University Park, PA 16802.
E-mail: deng@essc.psu.edu

and variety of shallow cloud systems. A two-layer model based on a mass flux approach was developed by Betts (1973) to study nonprecipitating cumulus convection. In that study, the convection-related processes of latent heating, dilution, mixing, and entrainment were investigated to predict the mean downward transfer of sensible heat in the cumulus layer. This, and similar models by Albrecht et al. (1979), Albrecht (1993), and Wang (1993), helped lay the foundation for a better quantitative understanding of the role of cumulus convection in trade wind atmospheres, including the impact of drizzle. However, although they represented the thermodynamic structure of the trade wind cloud-topped boundary layer (CTBL) reasonably well, the simple vertical structure of these models limited their adaptability for a wider range of cloud environments.

At the other extreme the rapid growth of computational resources in recent years has allowed detailed investigation of convective complexities using large-eddy simulations (LESs) having grid lengths of 100 m or less (e.g., Cuijpers and Duynkerke 1995; Siebesma and Cuijpers 1995; Rao 1996; Wyant et al. 1997). However, at present, the computational expense of LES prevents its use for regional-scale 3D domains. Nevertheless, LES is a useful tool for improving our understanding of turbulence-scale processes, which are crucial for the development of shallow-convection parameterizations suitable for larger-scale models.

Other approaches have proven useful for NWP models. For example, Betts (1986) and Betts and Bores (1990) proposed a combined shallow and deep cloud parameterization, with the shallow component based on a ''mixing line'' between subcloud and cloud-top air. This approach is currently used in the National Centers for Environmental Prediction's Eta Model (Black 1994) as well as numerous other research and NWP models. Multilayer mass flux schemes described by Tiedtke (1989) and Gregory and Rowntree (1990) are used in models at the European Centre for Medium-Range Weather Forecasts and the Met Office, respectively. These schemes are quite sophisticated, but appear to lack the flexibility for our needs, particularly in regard to air quality applications. For example, Gregory and Rowntree's approach mixes convective cloud water over the entire grid cell, rather than allowing it to remain in subgrid-scale cloud entities. The closure used in Tiedtke's parameterization is based on a balance between surface evaporation and the shallow-cloud moisture flux, which may not be appropriate over land.

In this paper, we describe a new parameterization of shallow convection designed primarily for mesoscale numerical weather prediction models, but adaptable to climate and air-chemistry models as well. The objective of this paper, then, is to develop a parameterization to represent the physical processes of shallow convective clouds and their influences on the mesoscale environment. Although intended for wider applicability, this development will be done within the framework of the fifth-generation Pennsylvania State University–National Center for Atmospheric Research (PSU–NCAR) mesoscale model (MM5). The scheme is designed to represent a full range of environments from quasi-steady marine stratocumulus and trade wind cumulus to nonsteady diurnally forced continental convection. Moreover, it allows transitions from shallow convection to either stratus or deep convection, and vice versa. This parameterization will also provide detailed information about convective-cloud fields that can be very useful for air quality studies, although the focus of this paper will be on the meteorological aspects of the scheme.

Section 2 of this paper describes the shallow-convection parameterization scheme developed at Penn State. Section 3 outlines a 1D version of the MM5 and the treatment of atmospheric radiation in the presence of subgrid clouds, while section 4 presents results of initial applications of the shallow-convection parameterization scheme in both marine and continental environments. A brief summary is given in section 5. A more complete evaluation of the shallow-cloud scheme using observations from a variety of cloud environments, plus sensitivity experiments related to key parameters, are presented in a companion paper (Deng et al. 2003, hereafter Part II).

2. The shallow-convection parameterization

The Kain–Fritsch (1990) deep-convection scheme is the progenitor for the present shallow-cloud development. In the Kain–Fritsch (KF) scheme, if a cloud updraft fails to reach a critical depth necessary to support rain (i.e., shallow cloud), it is assumed to disappear without having any impact at all on its environment. Here, we seek especially to describe how those shallow clouds grow and interact with their surroundings. The primary purpose of any convection scheme for shallow or deep clouds is to describe the turbulent vertical mixing that occurs at subgrid scales in the cloud layer. To be consistent with the Kain–Fritsch deep-convection scheme, we adopt the same equations for the turbulent vertical mixing that appear in Kain and Fritsch (1993). The major elements of the new shallow-cloud scheme are 1) a definition of initial cloud parcel characteristics and the convective trigger mechanism, 2) a convective-cloud submodel based on the parcel buoyancy equation, 3) closure assumptions that determine the cloud-base mass flux, and 4) a prognostic scheme for the area and water content of clouds that result from detrainment of the convective updraft air.

The shallow convection parameterization is designed to represent the physical linkage between the turbulent *planetary boundary layer* (PBL) and moist convective processes in a multilayer framework. We define the PBL as the layer beginning at the surface and extending upward to the point where surface-based turbulence rapidly decreases with height. Although the top of this layer can be identified in a model by the drop-off in turbulent kinetic energy, it also tends to be characterized quite often by a sharp jump in the potential temperature. Thus, it can be distinguished from the *cloud-topped boundary layer* (CTBL) discussed by some investigators (e.g., Albrecht 1979; Agee 1987), which includes the PBL plus a shallow-cloud layer having distinctly different stability characteristics.

We assume that shallow convective clouds consist of active updrafts and (approximately) *neutrally buoyant clouds* (NBCs). The NBCs represent either remnants of previous updrafts or the cloud mass dispelled from currently active updraft cores. This production of NBCs from detrained updraft air is consistent with the conceptual model of shallow convection presented by Wyant et al. (1997). The most vigorous convective updrafts generally cover less than 10% of a grid area, while the associated NBCs may cover a much greater fraction of the sky. The absence of significant vertical motions in the NBCs, compared to the positive vertical velocities in shallow-cloud updrafts on the order of 1–10 m s^{-1}, make them the more efficient pathway for the larger drops to fall as light rain or drizzle. Thus, the shallow convective updrafts are assumed to produce no rain, while the NBCs may generate some light precipitation. In general, most of the updraft mass is detrained near the cloud tops as it reaches or overshoots the equilibrium level of individual updrafts. Over time, this detrainment process and the consequent induced subsidence can change or even dominate the thermal and moisture structure of the mesoscale environment.

If the shallow-cloud updraft exceeds a critical depth (defined in the KF scheme as $D_{\mathrm{KF}} = 4$ km), it is considered to transition to deep convection (thunderstorm), often with heavy precipitation and strong moist downdrafts (Kain and Fritsch 1990). On the other hand, under conditions with a strong capping inversion and large vertical moisture flux, the detrainment process can lead to an accumulation of vapor and detrained cloud mass at the inversion base so that a solid stratus deck may develop. Thus, the shallow convection can have a direct link to both resolved stratiform cloud and subgrid deep convective cloud, both of which can be active precipitation generators. In many 3D models, representation of the physical relationships among these three types of cloud is weak at best.

a. Cloud-parcel initial characteristics

The parameterization is built as a one-dimensional column submodel. Active cloud updrafts are triggered when parcels originating in the PBL are able to reach their lifting condensation level (LCL). The characteristics of a potential cloud-initiating parcel are defined by its virtual potential temperature, θ_{vp}, and vertical velocity. The value of θ_{vp} for the parcel is defined at each time step from the average ambient values of the model layers in the lowest 20% of the PBL or in the lowest two model layers, whichever is deeper. The underlying assumptions are that energetic turbulent eddies are initiated near the surface and that the largest (and most buoyant) of these rise with only modest dilution through the entire PBL to approach or reach their LCL. The LCL for a parcel is calculated according to the method of Fritsch and Chappell (1980) and Chappell et al. (1974), and may lie below or above the PBL top. When the LCL is above the PBL top, the parcels must have sufficient momentum and initial buoyancy to penetrate the capping inversion if they are to reach saturation. Obviously, if none of the parcels can reach their LCL, the updraft area is zero. At the other extreme, when the LCL is inside the uppermost part of the PBL, all upward moving parcels are saturated and can be considered as convective updrafts, however shallow they may be. In that case, based on the probability density of upward motions on a horizontal slice through the upper part of the convective boundary layer in a LES (Weil 1988; Lamb 1982), it appears that the maximum possible updraft area can be ~30%–40%. In theory, an ensemble of shallow clouds could be created by defining parcels with different initial characteristics based on a similar probability distribution about the eddy vertical velocity and θ_{vp}, but that approach has not been introduced here.

Following eddy-transport theory, we hypothesize that these cloud-forming parcels have positively correlated thermal, moisture, and vertical velocity perturbations. The eddy vertical velocity, w_T, is defined from the maximum turbulent kinetic energy (TKE) anywhere in the PBL column according to

$$w_T = \sqrt{\frac{2}{3}\mathrm{TKE}_{\mathrm{MAX}}}, \tag{2.1}$$

where the constant 2/3 results from the TKE definition, assuming that the turbulence is isotropic. We then define the release height of the cloud initiating parcel, z_R, to be the lower of two levels: the top of the PBL (h_{PBL}) or the LCL. The total vertical velocity of the cloud-initiating parcel is estimated as $w_P = \overline{w} + w_T$, where $\overline{w}$ is the resolved-scale vertical motion at z_R. Thus, θ_{vp} and w_P define the thermal, moisture, and vertical velocity characteristics of the cloud initiating parcel at its level of release, z_R. The TKE and h_{PBL} are calculated using a 1.5-order turbulence scheme (Gayno 1994; Shafran et al. 2000). Typically, in a weakly forced marine boundary layer w_T is only ~0.1–0.3 m s^{-1}. Over land in a shear-driven nocturnal boundary layer, w_T may grow to ~0.3–0.8 m s^{-1}, while during the afternoon in a convectively unstable boundary layer it can easily reach 1–2 m s^{-1}. Vertical motion of the parcel following release, as well as its thermal and moisture properties, are calculated using the Kain–Fritsch (1990) entraining–detraining cloud model, based on the parcel buoyancy equation (also see below). If a cloud-initiating parcel becomes negatively buoyant and has too little vertical momentum to reach its LCL, it is assumed to return to its point of origin in the PBL without affecting the environment.

Additional factors (e.g., subgrid terrain irregularity or land-use variability) also may contribute to the parcel vertical velocity in certain cases, but most of these are ignored at present. However, a perturbation vertical velocity, w_{NH}, at the release height, z_R, is added to the initial velocity of the cloud-initiating parcel for the case of deep convection. The term w_{NH} is based on vertical accelerations forced by the growing nonhydrostatic pressure imbalances in a deep storm, as expressed in the third equation of motion. These storm-scale accelerations cannot be predicted directly because they occur at the subgrid scale. Thus, we assume that the induced upward velocity at z_R is proportional to the velocity in the accelerating updraft some distance above cloud base. The purpose of w_{NH} is to counter the effect of deep-convection feedbacks that can warm and dry the subcloud layer (before moist downdrafts develop), thereby shutting off the convection too early in the model. In effect, w_{NH} merely adds extra momentum to the initiating parcel so that the convection can continue until the KF deep convection reaches maturity. In shallow clouds, this factor is considered to be negligible. The relationship between the updraft acceleration and the nonhydrostatic pressure gradient forces beneath the deep-convective cloud has been discussed by Schlesinger (1984).

The relationship between w_{NH} and the vertical velocity in the updraft (calculated from the parcel buoyancy equation in KF; see below) is defined through an empirical proportionality constant. We invoke w_{NH} when the cloud depth D_c becomes greater than the critical Kain–Fritsch depth, $D_{KF} = 4$ km, that defines the threshold for producing convective rainfall. In this case, w_{NH} is defined as a simple function of $w(z_{2000})$, which is the updraft vertical velocity at 2 km above the cloud base, according to

$$w_{NH} = \begin{cases} 0.25[w(z_{2000}) - w_P] & \text{if } w(z_{2000}) - w_P > 0 \\ & \quad \text{and } D_C > D_{KF} \\ 0, & \text{otherwise.} \end{cases} \tag{2.2}$$

The parameter 0.25 in (2.2) was chosen after testing a range of values from 0.05 to 0.50. Since maximum expected value of $w(z_{2000})$ should be 10–20 m s^{-1}, this yields a maximum magnitude of w_{NH} in the range $2.5 < w_{NH} < 5.0$ m s^{-1} when deep convection is present. The total parcel vertical velocity at z_R, therefore, is given by

$$w_R = \overline{w} + w_T + w_{NH} = w_P + w_{NH}. \tag{2.3}$$

If the cloud-initiating parcel reaches the LCL, a convective-cloud updraft forms. Its subsequent acceleration and mixing with the environment are calculated using the entraining–detraining cloud model of Kain and Fritsch (1990). The entrainment rate at any level is a function of the radius of the updraft, R_C, and the local parcel buoyancy with respect to its environment (Kain and Fritsch 1990, 1993). While the Kain–Fritsch deep-convection scheme assumes a constant updraft radius of 1.5 km, the shallow-convection scheme allows the radius R_C to grow smoothly with time from a minimum of $R_{C\min} = 0.15$ km to a maximum of $R_{C\max} = 1.50$ km, which occurs when (if) the shallow convection transitions to deep precipitating convection. Although this approach is slightly more general than in the original Kain–Fritsch scheme, we note that Siebesma and Holtslag (1996) found that entrainment–detrainment rates in typical mass flux parameterizations for shallow convection often are underestimated by up to an order of magnitude. Grant and Brown (1999) have proposed a similarity hypothesis for shallow convection, based on TKE arguments, that can be used to determine a more flexible form for the entrainment rate. Recent tests by Gregory (2001) indicate that approaches like those of Grant and Brown (1999) and Siebesma (1997) indeed can provide more realistic entrainment–detrainment rate profiles for shallow convection. For the present, we adopt the original Kain–Fritsch approach, but note that future testing with more advanced entrainment–detrainment formulations is appropriate.

For our present purpose, we assume that the most significant factors controlling R_C are the boundary layer depth h_{PBL} and the cloud depth ($D_C = z_T - z_B$, where z_T is the height of cloud top and z_B = LCL is the cloud-base height). Of course, in reality there is considerable variability among individual members of the shallow cloud field. The relationship among these quantities and its variance perhaps could be defined best by analyzing a suitable range of moist LES results, but that is beyond the present scope and is left for future research.

Currently, a solution to a quadratic equation is used to express a general relationship between R_C, h_{PBL}, and D_C based on two common observations. First, as the boundary layer depth grows, the scale of its largest eddies broadens so that the mean radius of the cloud-initiating updrafts should expand. Thus, we expect the radius to scale most closely with the PBL depth for the shallower clouds (say, $D_C < 1$ km). Second, in most environments, the mean cloud-updraft radius is correlated positively with the depth of the convective clouds themselves. Thus, we also assume that, as the depth of the cloud updraft grows, the influence of D_C on the updraft radius should come to dominate over that of boundary layer depth. (The calculation of the cloud depth is described below in section 2b.) Three additional constraints are imposed. As $D_C \to 0$, we require $R_C \to$ 150 m (an arbitrary minimum radius) for all values of h_{PBL}. Also, as $D_C \to 4$ km, R_C must approach a constant maximum $R_{C\max} = 1.50$ km for all values of h_{PBL} for consistency with KF. Finally, since the parameterization is meant to apply only to shallow clouds driven by PBL processes, we insist that $R_C \to 150$ m as $h_{PBL} \to 0$. For simplicity, all updrafts in a grid cell are considered to have equal radius and depth at a given time. This uniform geometry is convenient, although an ensemble of different cloud sizes would be more realistic (e.g., Sie-

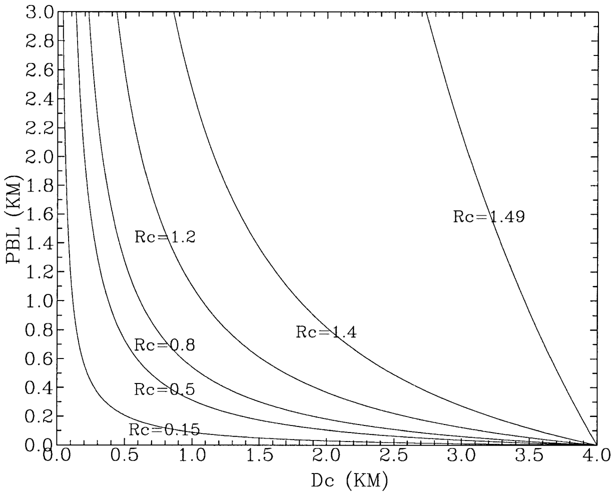

FIG. 1. Relationship between updraft radius (R_C, km), PBL height (h_{PBL}, km), and cloud depth (D_C, km).

besma and Cuijpers 1995). We express these basic assumptions and constraints on the cloud-updraft radius as a family of curves represented by the following quadratic solution (when $D_C < D_{KF}$):

$$R_C = \frac{b - \sqrt{b^2 - 12\eta h_{PBL}}}{4} \quad \text{for } R_{C\,\min} \le R_C \le R_{C\,\max}, \tag{2.4}$$

where $b = (7 + 2\eta h_{PBL})/2$, $\eta = 12D_C/(4 - D_C)$, and R_C, D_C, and h_{PBL} are in kilometers

Figure 1 demonstrates the relationship between R_C, D_C, and h_{PBL} resulting from (2.4). For deep boundary layers, as might be found over land, notice that even fairly shallow clouds quickly expand to have large radii as the updraft depth begins to grow (e.g., $R_C > D_C$ for $h_{PBL} = 2.0$ km and $D_C = 1.0$ km). For very shallow boundary layers, the clouds must become quite deep before large radii develop (e.g., $R_C < D_C$ for $h_{PBL} = 0.4$ km and $D_C = 2.0$ km). This latter condition (relatively tall and narrow convective updrafts initiated from a shallow boundary layer) is expected to be less common over land, but may occur in tropical or subtropical marine environments. The effect of the three limiting constraints on the updraft radius is evident in the figure. Also, it should be noted that (2.4) applies to the geometry of a shallow-cloud updraft, not the visible cloud, which can be very different (see sections 2d and 4). When $D_C \ge D_{KF}$, thermodynamic control is passed to the KF deep convection scheme, which includes convective rainfall and moist downdraft development. The specific formulation used in (2.4) is meant to express only qualitative relationships based on the assumptions and constraints, but the resultant cloud distributions appear to be fairly consistent with general shallow convective-cloud observations. The application of R_C was most effective when averaged over two to three time steps.

b. The convective-cloud submodel

As mentioned in section 2a, the formulations of KF 1D entraining–detraining cloud model are used to calculate the updraft vertical velocity and the convective thermal and liquid-water profiles every time step based on the parcel buoyancy equation. The form of the KF vertical velocity equation is essentially the same as that used by Simpson and Wiggert (1969) and Kreitzberg and Perkey (1976), except that the ‘‘form drag’’ term that they use is not included. Unlike KF, however, clouds are not assumed to grow instantly to their mature equilibrium level as soon as a cloud is triggered. Here, the cloud top grows gradually at a rate proportional to the maximum vertical velocity of the updraft between levels z_B and z_T, identified as $W_{\max}$, and is estimated to be

$$\frac{dz_T}{dt} = 0.2W_{\max} \tag{2.5}$$

until the equilibrium level is reached. The empirical factor 0.2 imposes a reasonable cloud growth rate (e.g., see Simpson 1983) so that, under deep-convection conditions, it usually takes 20–30 min to reach the tropopause from the level of free convection (LFC). This approach allows detrainment from the growing cloud top to moisten the environment, which is oversimplified in the instantaneous cloud growth of the KF scheme. The interpretation of the 0.2 factor is that cloud-top growth is slowed because the updraft must do work against (push aside) environmental air to continue its upward progress, while the parcel buoyancy equation merely describes the cloud's velocity profile in its full-grown state. If the updraft top, z_T, exceeds the equilibrium level at any time, it is adjusted downward immediately and the updraft mass is detrained into the NBC (also see section 2d).

Although the thermal and moisture characteristics of the cloud-forming parcel are defined from the lowest 20% of the PBL (section 2a), its mass is taken directly from the subcloud layers nearest to the cloud base. The depth of this updraft source layer, D_S, grows as a function of the updraft radius from a minimum of 100 m to a maximum of 600 m according to

$$D_S = d_1 + 1000(R_C - R_{C\,\min})/d_2 \tag{2.6}$$

with the constraint $D_S \le h_{PBL}$ and where $d_1 = 100$ m and $d_2 = 2.7$. Thus, as clouds grow wider and deeper they are expected to have greater mass flux at cloud base and are likely to entrain air from a deeper subcloud layer. The maximum D_S of 600 m is chosen to match the constant value used in KF for deep convection. To satisfy continuity requirements, subsidence is induced in the cloud environment to compensate for the mass extracted from the PBL source layer. If the cloud remains ‘‘shallow,’’ ($D_C < D_{KF}$), no subgrid scale convective downdrafts are allowed to form, so all compensation for the upward mass flux must occur through this subsidence mechanism.

It should be noted that, although the growth of the updrafts occurs gradually, only one size of clouds is allowed in a particular grid column in the present formulation. That is, unlike the atmosphere, we do not attempt at this time to represent an ensemble of cloud sizes, as has been done in the convection scheme by Arakawa and Schubert (1974). In effect, the parameterization represents the deepest convective clouds that are expected to dominate the feedbacks to the environment (also see section 2c).

c. Cloud updraft closure assumptions

The cloud-base mass flux closure is adopted to determine the intensity of subgrid convection from resolved-scale quantities. The grid-cell mass flux at cloud base is defined as

$$\mu_B = N(\pi R_C^2 \rho w_B), \tag{2.7}$$

where N is the number of updrafts in the cell, w_B is the parcel vertical velocity at cloud base, and ρ is the parcel air density (here, R_C is in m). Generally, closure requires that either μ_B or N must be specified to allow the other quantity to be diagnosed. Of course, for any scheme, errors may occur in the calculation of N, R_C, or w_B, but the key is to estimate μ_B with reasonable accuracy so as to simulate realistic measurable cloud-field characteristics (e.g., cloud fraction, depth, liquid-water pathlength, etc.). Moreover, as stated above, we have made the simplifying assumption that all shallow clouds in a grid cell have the same geometry, rather than use a more realistic distribution of cloud sizes. Thus, the calculations for N and R_C, in particular, should not be considered literal, but merely provide a qualitative estimate needed for the mass flux calculations.

As part of the preliminary development of the updraft module for the shallow-convection scheme, five different mass-flux closure assumptions were tested. Brief descriptions and comments about these closures are as follows:

1) BOUNDARY LAYER VAPOR BALANCE (BLVB)

Used by Tiedtke (1989) to simulate subtropical trade cumuli, this closure assumes total water vapor in the PBL is constant (in the absence of rain). That is, the rate of vapor removal from the PBL by cloud-base updrafts is balanced by the sum of surface evaporation and the vapor entrainment flux at the PBL top. Thus, N_1 (the number of cloud updrafts for the BLVB closure) can be diagnosed from (2.7) by defining $q_v\mu_B$ as the sum of these two fluxes. Although the BLVB closure was found to be reasonable for many marine environments, it greatly underestimated the cloud-base mass flux in continental applications (not shown) and therefore was eliminated from further consideration.

2) CONVECTIVE AVAILABLE POTENTIAL ENERGY (CAPE) REMOVAL

This closure assumes that total cloud-base mass flux proceeds at a rate necessary to stabilize the column over a deep-convective time period, which is generally about 30 min (Fritsch and Chappell 1980; Kain and Fritsch 1990). Similar to the BLVB closure, the CAPE-removal closure diagnoses the number of updrafts in the grid cell, N_2, from (2.7) using the CAPE-derived μ_B. The CAPE closure often works poorly in shallow-convection environments where the cloud depths are about 1 km or less (i.e., there is little or no CAPE in the shallow-cloud layer). Nevertheless, it is still attractive for cases in which most of the shallow cloud lies above the LFC. Application of N_2 was found to be most effective when averaged over $\sim$15 time steps.

3) BOUNDARY LAYER DEPTH (BLD) RELATIONSHIP

This closure assumes that the number of updrafts for a shallow-convection environment, N_3, is a direct function of the scale of the largest, most energetic turbulent eddies in the PBL. Thus, N_3 depends on the depth of that layer. Since the maximum amplitude of the eddy vertical velocity spectra occurs at wavelength $\sim 1.5h_{\mathrm{PBL}}$ (Young 1987), we hypothesize that under convective conditions, this geometry can be used to estimate the distribution and number of cloud-initiating updrafts in a grid cell according to

$$N_3 = b_3 \frac{\Delta x \Delta y}{(1.5h_{\mathrm{PBL}})^2}, \tag{2.8}$$

where $\Delta x \Delta y$ is the grid-cell area. The total mass flux, μ_B, can then be calculated from (2.7). The maximum number of clouds possible from (2.8) would occur for $b_3 = 1.0$, which would imply a fully developed shallow-cloud updraft exists at every potential initiating site in the grid cell (i.e., at horizontal intervals of $1.5h_{\mathrm{PBL}}$). However, that certainly would overestimate the number of active updrafts. Tests run for a range of $0.01 < b_3 < 1.0$ indicated that $b_3 = 0.025$ was a reasonable estimate for this constant. Note that smaller clouds or NBC remnants of old updrafts are not counted in N_3. A similar closure has been used by other investigators to study boundary layer rolls (Stull 1988), so (2.8) could be modified for use in strongly sheared environments. The BLD closure was tested in both continental and marine environments and found to be suitable for fairly shallow cloud depths ($D_C < 2$ km). However, it sometimes caused large oscillations in the mass flux due to feedbacks among h_{PBL}, N_3, and μ_B.

4) TKE-BASED CLOSURE

This closure operates on the assumption that shallow clouds basically are driven by the TKE in the PBL. Specifically, it scales the shallow-cloud updraft mass flux, μ_B, by the magnitude of the maximum diagnosed TKE in the subcloud mass-source layer, TKE_1. We can express this closure as

$$\mu_B = \left(\frac{\mathrm{TKE}_1}{\mathrm{TKE}_C}\right)\mu_B(\max). \tag{2.9}$$

The term $\mu_B(\max) = M_S/\tau_{SC}$ is the mass flux required to evacuate the total mass in the subcloud layer, M_S, over a relaxation timescale defined as $\tau_{SC} = D_S/w_B$, where D_S is the depth of the subcloud source layer. Thus, for a typical cloud base at 1200 m and a cloud-base updraft of 1 m s^{-1}, the relaxation timescale represents the time (20 min) in which all of the mass below cloud base could be evacuated, assuming the entire grid cell experiences w_B (i.e., the cell is covered by one large updraft) and assuming no compensating mass flux into the layer. Of course, since w_B applies only in the subgrid area of the updrafts, $N\pi R_C^2$, the actual mass flux is considerably less than the potential maximum value $\mu_B(\max)$. A dimensional constant, TKE_C, in (2.9) expresses the proportionality between μ_B, $\mu_B(\max)$, and TKE_1.

To obtain the number of clouds in the grid cell from (2.9), we first substitute for the total subcloud mass, $M_S = \rho\Delta x\Delta y D_S$, and for τ_{SC} in the relationship for $\mu_B(\max)$ to obtain

$$\mu_B(\max) = \Delta x\Delta y\rho w_B. \tag{2.10}$$

Substituting (2.9) and (2.10) into (2.7), we solve for the number of clouds in the grid cell

$$N_4 = \left(\frac{\Delta x\Delta y}{\pi \mathrm{TKE}_C}\right)\frac{\mathrm{TKE}_1}{R_C^2} = C_1\frac{\mathrm{TKE}_1}{R_C^2}. \tag{2.11}$$

Experimentation in both marine and continental environments indicated that $\mathrm{TKE}_C = 45$ J kg^{-1} can be used for the proportionality constant. For a given model grid, note that $C_1 = \Delta x\Delta y/\pi\mathrm{TKE}_C$ can be treated as a constant, so (2.11) reveals N_4 to be a simple time function dependent only on TKE_1 and R_C. An empirical constraint of $1.0 \le \mathrm{TKE}_1 \le 10.0$ is placed on the maximum TKE in the subcloud layer to complete the mass flux closure. The lower limit on TKE_1 has the effect of further simplifying N_4 to be a function only of R_C in weakly forced environments, such as marine trade wind cumulus conditions. These bounds on TKE_1 are likely to be somewhat dependent on the specific turbulence scheme used in conjunction with the shallow-convection submodel, perhaps requiring some recalibration for use with alternative schemes. Tests of the TKE-based closure showed it to operate well for most shallow clouds ($D_C < 2$ km), while it damped most of the feedback oscillations that were characteristic of the BLD closure.

Moreover, concerning this TKE closure, we have noted that it is possible to represent the eddy vertical motions in a turbulent boundary layer by a normalized probability distribution (e.g., Lamb 1982) and that the area under this distribution can be considered proportional to the total shallow-convection updraft area. Assuming that the LCL lies in or above the inversion layer, it is typical for only a few parcels with stronger than average upward motion to reach the LCL, so we can call the minimum velocity leading to a cloud $w_{\min}$ (with initial parcel buoyancy viewed as a ''potential velocity'' through the third equation of motion). From (2.1), it is easily seen that the initial vertical velocity of the most energetic parcels, $\sim w_b$, scales to $\sqrt{\mathrm{TKE}_1}$. However, the probability of parcels having sufficient energy to reach the LCL is not merely a function of w_b, but is proportional to the area under the portion of the vertical-velocity probability distribution that lies to the right of the minimum velocity, $w_{\min}$. As TKE_1 grows and assuming $w_b > w_{\min}$, this area must grow much faster than w_b. Thus, we make a first guess that the area is proportional to w_b^2, which then scales to $\mathrm{TKE}_{\max} \sim \mathrm{TKE}_1$. Given the bounds $1 < \mathrm{TKE}_1 < 10$ J kg^{-1} and noting that in (2.9) the term $\mathrm{TKE}_1/\mathrm{TKE}_C$ is effectively the total updraft area in a grid cell, this closure gives a range of possible updraft area for the shallow convection scheme as $0.022 < N_4\pi R_c^2/\Delta x^2 < 0.22$. Since in practice $\mathrm{TKE}_1 < 3$ J kg^{-1} for most situations, the effective range for total updraft area becomes $0.022 < N_4\pi R_c^2/\Delta x^2 < 0.066$. Although this is a reasonable range, the assumptions made here need to be examined more thoroughly in future work.

5) Hybrid closure

Since the TKE-based closure was found to work well for fairly shallow convective clouds and the CAPE-removal closure was found to work better for deeper clouds (D_C approaching D_{KF}), a simple hybrid closure is proposed to represent the intermediate range of cloud depths. When cloud tops are above the LFC, but have depths less than D_{KF} (which describes a large percentage of convective cases), the clouds are assumed to be in transition from the TKE-based closure to the CAPE-removal closure. A simple linear averaging is used in this case, although refined transition functions could be hypothesized. First, the number of updrafts is calculated according to each of the two closures (N_2 and N_4). Then, the final number of updrafts is estimated based on the fraction of the cloud depth that lies above the LFC relative to the distance between the LFC and the height D_{KF} above cloud base, given by

$$N = fN_2 + (1 - f)N_4, \tag{2.12}$$

where $f = h_3/h_1$ is a ratio of two length scales (km) such that $h_3 = D_C - h_2$, $h_1 = D_{KF} - h_2$. Here, $h_2 = z_{LFC} - z_B$, and z_{LFC} is the height of the LFC. Normally, $N_2 < N_4$ because the CAPE-removal closure hypothesizes that stabilization of a deep cloud layer occurs rather rapidly as a result of a few vigorous updrafts. This agrees with the general observation that the number of growing clouds in an area decreases as their size (depth and width) increases.

To summarize, the shallow-convection parameterization may use any of three mass-flux closure assumptions (type 2, 4, or 5), determined by D_C, z_T, and z_{LFC}, according to

$$\begin{aligned} &z_T \le z_{\mathrm{LFC}} && \rightarrow \text{TKE-based closure only} \\ &z_T > z_{\mathrm{LFC}},\ D_C < D_{\mathrm{KF}} && \rightarrow \text{Hybrid closure} \\ &D_C \ge D_{\mathrm{KF}} && \rightarrow \text{CAPE-removal closure only,} \end{aligned} \tag{2.13}$$

which provides a smooth transition from one closure to another as the cloud depth grows. Results of experiments to explore the sensitivity of the hybrid closure to cloud updraft radius, R_C, appear in Part II. It also should be remembered that the uniform updraft geometry used in the present formulation represents a simplification (i.e., it treats only the largest cloud at a given time, which should dominate the mass flux), while the atmosphere typically exhibits an ensemble of cloud depths (also see section 2b). Using LES, Siebesma and Cuijpers (1995) showed that a variety of cloud sizes skews the level of maximum mass flux downward and contributes to a reduction in the updraft mass flux with height. While this effect is not considered in the present version of the parameterization, their LES results suggest that the updraft mass flux could perhaps be modified to account for a distribution of cloud sizes.

d. Prognostic scheme for neutrally buoyant cloud fraction and cloud water

The parameterizations described in sections 2a–c describe the initialization, closure assumptions, and growth of the shallow-cloud updrafts. Updrafts are assumed to detrain all mass after each time step and their characteristics are recalculated on the following time step. Thus, the cloud characteristics are able to evolve rapidly as the environment changes due to cloud feedbacks and other forcing in the model. This does not mean that a new cloud updraft must begin to grow from the LCL after every time step. Instead, the cloud top continues to grow from its height at the previous time step according to (2.5) so that continuity is maintained for the updraft characteristics. In the event that z_T exceeds the equilibrium level at the new time step, z_T is redefined downward to the equilibrium level. However, the mass detrained from the updraft must be accounted for.

Most cloud parameterizations designed for the mesoscale consider only deep convection in detail. In these schemes, detrained cloudy air generally is fed back directly to the resolved scale, where it evaporates immediately until the grid cell saturates (e.g., Kain and Fritsch 1993). This ''all-or-nothing'' approach for post-convective layer-cloud formation is an oversimplification and can have negative impacts on other aspects of model performance, such as radiative processes and latent heating. In deep thunderstorms, large detrainment rates near the tropopause often cause a small- to moderate-sized grid cell ($\Delta x \le 25$ km) to saturate quite rapidly, so little damage is done by neglecting subgrid layer clouds. However, in the case of smaller shallow clouds, it may take many hours (if ever) for detrained cloud water to saturate a layer.

A more realistic representation is to detrain convective cloud mass from updrafts into a class of subgrid clouds having nearly neutral buoyancy (e.g., Wyant et al. 1997). Once the detrained updraft air becomes part of these subgrid NBCs, it can spread as layer clouds, initiate light precipitation, or slowly evaporate into the subsaturated grid volume. While some existing schemes have attempted to treat this detrained cloud mass in large-scale models (e.g., Tiedtke 1989, 1993), they often rely on a moisture-balance closure and so may not be versatile enough for both continental and marine environments.

1) BASIC EQUATIONS

The continuity equations for the rate of change of subgrid cloud area (a) and cloud water/ice content (l_c) for the NBCs are given by

$$\frac{\partial a}{\partial t} = S_a + D_a - \mathbf{v}\cdot\nabla_H a - w\frac{\partial a}{\partial z}, \tag{2.14}$$

$$\frac{\partial l_c}{\partial t} = S_l + D_{\mathrm{mix}} + D_{\mathrm{pre}} + D_{\mathrm{ics}} + D_{\mathrm{CTEI}} - \mathbf{v}\cdot\nabla_H l_c - w\frac{\partial l_c}{\partial z}. \tag{2.15}$$

Here S_a and S_l are sources of cloud area and condensed water content ejected from convective updrafts, respectively. The term D_a (dissipation of cloud area) represents evaporation due to mixing at the sides of the cloud; D_{mix} is the depletion of water liquid/ice content due to vertical mixing; D_{pre} is water depletion due to precipitation (drizzle); D_{ics} is a depletion rate contributed by an ice settling process; and D_{CTEI} is water depletion due to cloud-top entrainment instability. The horizontal and vertical advection terms are represented by $-\mathbf{v}\cdot\nabla_H\chi$ and $-w\partial\chi/\partial z$, where χ is either l_c or a. The grid-averaged condensed water content (l) is related to the subgrid NBC water content (l_c) according to $l = al_c$. When $a = 1.0$ (saturated conditions), then $l = l_c = q_c$, where q_c is the model's explicit (resolved scale) cloud-water mixing ratio.

2) FORMATION OF NEUTRALLY BUOYANT CLOUDS

Convection produces a variety of clouds either directly, such as cumulus and cumulonimbus, or indirectly, such as stratocumulus and anvils. A realistic parameterization for clouds of convective origin, but which have nearly neutral buoyancy, is obtained by considering their source to be condensates produced in subgrid cumulus updrafts (active convective clouds) and later detrained at the subgrid scale into the nonconvective environment. The following equations represent the source terms for the subgrid NBCs described in (2.14) and (2.15):

$$S_a = -\tilde{w}\frac{\partial a}{\partial z} + \frac{R_{\mathrm{ud}}}{M_L} \tag{2.16}$$

$$S_l = \frac{\left(\dfrac{\partial l}{\partial t} - l_c S_a\right)}{a}, \tag{2.17}$$

where

$$\frac{\partial l}{\partial t} = -\tilde{w}\frac{\partial l}{\partial z} + \frac{R_{\mathrm{ud}}}{M_L} l_u. \tag{2.18}$$

Here $\tilde{w}$ is the convection-induced subgrid-scale subsidence, R_{ud} (kg s^{-1}) is the updraft detrainment rate from the parcel-buoyancy scheme, and M_L(kg) is total mass of air in a grid cell for a given model layer. The liquid/ice water content in the updraft core is given by l_u. Note that the volume of detrained updraft air increases the area of the NBC (a), while its liquid water content (l_c) is solved as a residual term in (2.17) to satisfy the mass conservation constraint $l = al_c$.

3) Evaporation of clouds

In (2.14) and (2.15), there are several processes through which the NBC can dissipate. Following Tiedtke (1993), the area decreases through cloud-edge evaporation according to

$$D_a = -\frac{a}{l_c} K(q_s - q_v), \tag{2.19}$$

where $K = 10^{-5}$ s^{-1} is a horizontal diffusion coefficient, and q_v and q_s are the resolved-scale specific humidity and saturation specific humidity, respectively. This yields a dissipation timescale on order of a day for $l_c = 1.0$ g kg^{-1}. Notice however that, by taking l_c into account, the ''effective'' diffusion coefficient for the cloud area becomes K/l_c. Thus, the dissipation rate becomes significantly greater when the cloud water content becomes small ($l_c < 0.1$ g kg^{-1}). Consequently, this term accounts for the final dissipation of clouds from which most of the condensate has already been depleted by other processes.

4) Depletion of water liquid/ice content by in-cloud mixing processes

Inside the NBC, cloud water in the submodel can be mixed downward (but not upward) by vertical diffusion induced by turbulence and radiation flux divergence, given by

$$D_{\mathrm{mix}} = \frac{1}{a}\frac{\partial}{\partial z}\left[(K_v + K_r)\frac{\partial(al_c)}{\partial z}\right], \tag{2.20}$$

where K_v is the local diffusion coefficient derived from the TKE. The additional radiation-induced diffusion coefficient is given by

$$K_r = \frac{l_B^2}{\theta}\left[\left|\frac{\partial\theta}{\partial t}\right|_{\mathrm{LW}}\left|\frac{\Delta z_T}{15}\right| + \left|\frac{\partial\theta}{\partial t}\right|_{\mathrm{SW}}\left|\frac{\Delta z_T}{50}\right|\right], \tag{2.21}$$

where K_r is a maximum at the cloud top and decreases linearly downward over a maximum cloud depth of 1000 m. In (2.21), l_B is the Blackadar length scale provided by the turbulence scheme (Shafran et al. 2000), θ is the potential temperature of the environmental air and Δz_T is the model layer thickness at cloud the top. The terms $\partial\theta/\partial t|_{\mathrm{LW}}$ and $\partial\theta/\partial t|_{\mathrm{SW}}$ are the longwave cooling rate at cloud top and the daytime solar heating just below cloud top, respectively, provided by the radiation scheme. This K_r term would be unnecessary if very high vertical resolutions were possible, but in typical mesoscale models with $\Delta z_T \geq 50$ m, it accounts for radiation-induced turbulence occurring at scales that are too small to be represented accurately by K_v, which is derived from grid-resolved quantities in the turbulence scheme.

Cloud water also can evaporate into clear air at the exposed cloud base through the same vertical diffusion terms. The finite differenced form of these terms is one-sided so that the water flux is downward only. Thus, they prevent overentrainment of dry air into the upper part of the NBCs and overmixing of water into the environment above the clouds. Instead, the important entrainment process across the upper boundary of the cloud is represented using a cloud-top entrainment instability (CTEI) formulation described below. The one-way diffusion of cloud water in (2.20) is used primarily to accelerate the evaporation of clouds having low water content. It represents the most important water depletion process when the liquid/ice content is in the range of $0.1 < l_c < 0.5$ g kg^{-1}, where neither subgrid precipitation [section 2d(5)] or horizontal diffusion processes [section 2d(3)] are effective.

5) Precipitation processes

Precipitation can form in the NBCs through autoconversion and accretion, exactly as for resolved-scale layer clouds. Here, we use the simple water/ice cloud scheme of Dudhia (1989), without a mixed phase, for which autoconversion begins at $l_c > 0.5$ g kg^{-1} (a similar threshold exists for initiating autoconversion of ice, based on activation of ice nuclei below 273 K). It is feasible to introduce a mixed-phase explicit precipitation scheme for use with the shallow-convection scheme, but that is not done here. Also, cloud ice particles are assumed to fall slowly through an ice settling process described by Grell et al. (1994). The ice settling prevents long-term retention of low-density cirrus clouds that are unable to produce significant snowfall rates.

6) Cloud-top entrainment instability (CTEI)

Deardorff (1980) and Randall (1980) proposed that shallow clouds can dissipate through a mechanism called cloud-top entrainment instability. If a parcel of dry air is entrained into the cloud top, it induces mixing and evaporation. As a result, the density of the parcel may become greater than (θ_v less than) that of surrounding cloudy air, causing unstable acceleration of the parcel downward through the cloud. The depletion rate of the cloud liquid due to the CTEI, following Randall (1980) and Del Genio et al. (1996), is parameterized as

$$D_{\mathrm{CTEI}} = -10^{-4}\frac{r - r_{\min}}{r_{\max} - r_{\min}}l_c. \qquad (2.22)$$

Randall (1980) shows that $r = \Delta h/[L\Delta(q_v + l_c)]$, where the moist static energy is given by $h = C_P T + gz + Lq_v$, Δh represents the jump of h across the cloud top, $\Delta(q_v + l_C)$ is the jump of total water across the cloud top, L is the latent heat of vaporization, and C_P is the specific heat at constant pressure. In (2.22) $r_{\min}$ and $r_{\max}$ are CTEI initiation criteria given by Randall (1980) and MacVean and Mason (1990). If $r \leq r_{\min}$, then r is set equal to $r_{\min}$ and the depletion rate goes to zero; if $r \geq r_{\max}$, then r is set equal to $r_{\max}$, which gives the maximum depletion rate, $-10^{-4}\, l_C$ kg kg^{-1} s^{-1}. Because CTEI-induced downdraft cooling is expected to be confined to the upper portion of the cloud layer (Randall 1980), the depletion due to CTEI is applied only in the uppermost 100 m of the NBC.

Deardorff (1980) originally proposed CTEI as a possible dominant mechanism for the breakup and evaporation of a stratus deck. Although subsequent observational and modeling research has suggested that this is generally not the case, the process is included in the NBC submodel as a contributing factor for cloud water depletion.

3. The 1D MM5 model

The shallow-convection parameterization has been installed in a 1D version of the Penn State–NCAR mesoscale model, which is based on the nonhydrostatic numerical framework of the 3D parent model (Grell et al. 1994). In addition to the shallow-convection scheme, the 1D model contains a full set of MM5 physical parameterizations, including a 1.5-order turbulence submodel (Shafran et al. 2000), a Blackadar surface energy budget (Grell et al. 1994), an explicit moisture scheme (Dudhia 1989) that predicts resolved-scale liquid/ice cloud and precipitation, and a two-stream broadband column radiation submodel (Dudhia 1989). As discussed in section 2, it also contains the KF (1990) deep convection parameterization. Moreover, the user can specify 3D large-scale dynamical tendencies, such as advection and subsidence. Of these, the interaction between the shallow convection and radiation requires special note.

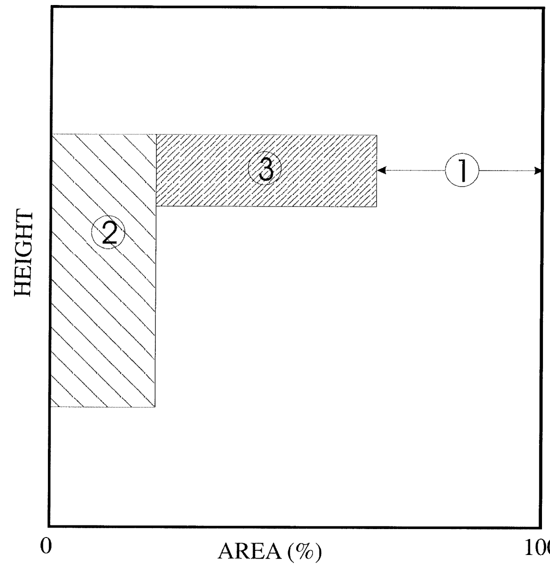

FIG. 2. Schematic diagram showing idealized partition of NBC in a grid column into 1) clear, 2) upright cloud, and 3) anvil cloud.

To function correctly with the shallow convection submodel, the radiation scheme must be applied separately to the subgrid clear and cloudy areas of the column. Like many other schemes, however, Dudhia's radiation assumes that a grid cell is either totally clear or totally cloudy. Furthermore, the shallow-cloud area predicted by (2.14) is a function of height. To solve this problem efficiently, the column's subgrid NBC is partitioned into three idealized parts (see Fig. 2): 1) clear throughout the model depth, 2) subgrid upright cloud through the full depth of the convective layer (often this is a fairly small fraction of the grid area), and 3) broad stratiform subgrid cloud (often near the top of the convective updraft, referred to here as the ''anvil'' for convenience). The radiation-induced thermal tendencies are calculated and applied separately to each fraction of the cell area. The convective updraft is detrained completely into the NBC after each time step, and so does not contribute to the radiative tendencies. Deng (1999) gives details of the methodology used for the subgrid partitioning represented in Fig. 2.

However, when the partitioned subgrid cloud areas 2 and 3 in the figure ($\overline{a}_2$ and $\overline{a}_3$) were used directly for the radiation calculations, the cloud effects on solar radiation estimated by the model were biased. That is, while the cloud-fraction calculations using (2.14) (see section 2d) gave good results in terms of the cloud-base mass flux and observed cloud characteristics (see Part II), the solar radiation penetrating beneath the cloud layer was overestimated. Therefore, another effect not related to the mass flux, but affecting the visible cloud area, must be treated improperly by the direct partitioning assumption described above.

We propose that the ‘‘effective’’ cloud fraction for the purpose of calculating the net effect of subgrid clouds on radiation (i.e., similar to the area as viewed from above) must be somewhat greater than the idealized distribution shown in Fig. 2. This occurs because (2.14) and the partitioning method described in Fig. 2 implicitly assume that clouds in adjacent layers always have the maximum possible overlap in the vertical. While this maximum-overlap assumption may give a reasonable first guess for clouds of convective origin, it is not likely to be accurate in general because in nature many dissipating NBCs are no longer linked vertically by an active updraft. An additional fractional area, a_s, is postulated to be a function of the environmental relative humidity in the cloud-free portion of the cell, RH, so that the total or ‘‘effective’’ cloud fraction, a_e, can be written as

$$a_e = (1 - a)a_s + a, \tag{3.1}$$

where a is the fraction predicted using (2.14). Following Xu and Randall (1996), the additional fraction, a_s, is parameterized according to

$$a_S = \mathrm{RH}^{\alpha_1}\left[1 - \exp\left(\frac{-\alpha_3(l_c + q_c)}{[(1 - \mathrm{RH})q_S]^{\alpha_2}}\right)\right] \quad \text{if RH} < 1, \tag{3.2}$$

where $a_S = 1$, if RH ≥ 1, and α_1, α_2, and α_3 are empirical constants they define as 0.25, 0.49, and 100, respectively. Note that the cloud liquid/ice content used in (3.2) appears as the sum of the cloud liquid/ice at the subgrid scale, l_c, and the resolved scale, q_c. However, when a layer becomes saturated, l_c converts into q_c, while $q_c = 0$ when the layer is subsaturated, so only one of these two quantities can actually be nonzero at a given time. The use of RH in the cloud-free portion of the grid cell to estimate the degree of nonoverlap of the NBC layers, a_S, is justified briefly as follows. In a dry environment, the NBCs are expected to be short-lived so that those that do exist will be tied closely to upright active updrafts (i.e., the visible NBCs will tend to be upright, as well). However, in a moister environment, the NBCs should be longer lived. Since they can last well after the individual updrafts cease, they can more easily become tilted or fragmented in a sheared environment, thereby causing a_S to become greater.

As an example, Fig. 3 shows the resultant area of the effective cloud, a_e (thin solid curve), in a marine stratocumulus case where the maximum predicted cloud area from (2.14) is $a_{\max} = 0.44$ (shaded region) and $\mathrm{RH}_{\max} = 0.93$ (heavy solid curve) at 1451 m. Notice that, in the cloud layers with lower relative humidity (0.85–0.90), the effective cloud fraction is only about 5%–10% greater than the calculated NBC fraction.

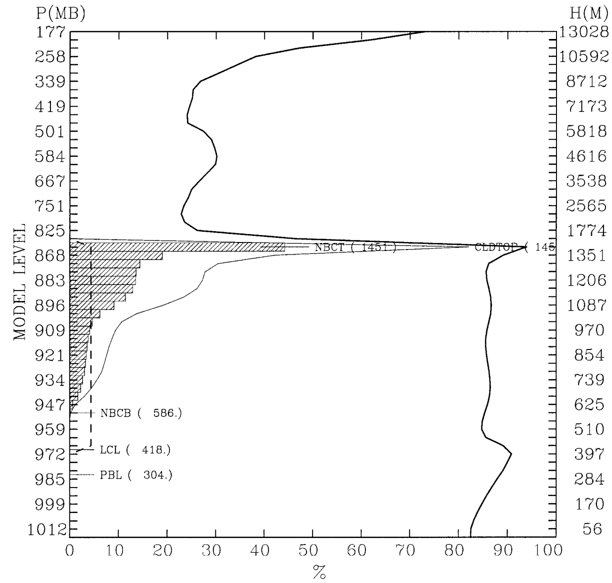

FIG. 3. Model-predicted cloud fraction (%) and resolved-scale relative humidity, RH (%), vs pressure (mb) and height (m) at 1200 UTC 11 Jun 1992 (hour 5) for ASTEX at 28.00°N, 24.22°W. Shading indicates NBC fraction (%), the dashed line is the area of shallow-cloud updraft (%), the thin solid curve is the effective cloud area for radiation calculations (%), and the heavy curve is RH (%). LCL denotes the lifting condensation level, PBL is the boundary layer top, CLDTOP is top of updraft, and NBCT and NBCB are the top and base of NBCs, respectively.

However, near the cloud top, where the relative humidity is greatest, a_e exceeds the NBC fraction by nearly 40%.

The surface radiation flux, R_S, (for either LW or SW flux) is given by

$$R_S = \overline{a}_{e2}R_2 + \overline{a}_{e3}R_3 + (1 - \overline{a}_{e2} - \overline{a}_{e3})R_{\mathrm{clr}}, \tag{3.3}$$

where $\overline{a}_{e2}$ and $\overline{a}_{e3}$ are the vertically averaged effective cloud fractions and R_2 and R_3 are the surface fluxes contributed from the subgrid upright and anvil portions of the NBC, respectively. The term R_{clr} is the surface flux contributed by the clear portion of the grid element.

4. Preliminary 1D model applications

This section briefly demonstrates initial applications of the shallow-convection scheme in both marine and continental environments. For more detailed verifications against measured cloud properties and an examination of the scheme’s sensitivity to key parameters, the reader is directed to Part II of this paper. In the marine environment, a case is chosen from the Atlantic Stratocumulus Transition Experiment (ASTEX), described by Albrecht et al. (1995). For the continental example, an anticyclonic case with shallow cumuli in the vicinity of Pittsburgh, Pennsylvania, is presented. All experiments use the 1D nonhydrostatic MM5 with 62 vertical levels, including 40-m resolution from the surface to 1400 m above ground level (AGL). Layer thicknesses gradually increase above this height to the top of the model at 100 mb. The nominal horizontal grid size is 30 km (used in calculating the number of clouds per grid cell) and the time step is 90 s.

a. Marine environment

A composite observed sounding from Betts et al. (1995) is used to provide typical initial conditions for the 1D MM5 in a quasi-steady subtropical marine environment (Fig. 4), while filtering out diurnal transients. The objective of this experiment is to demonstrate that the shallow-convection scheme can maintain clouds in a quasi-steady state over several days when subjected to the steady, moderate surface and radiative forcing of the mid–Atlantic Ocean. This is an important early milestone in testing the parameterization.

The composite was calculated using data collected during ASTEX for the period 11–14 June 1992 in the vicinity of the Azores Islands (28.00°N, 24.22°W). Dominated by the persistent Bermuda high, this region exhibits deep tropospheric subsidence and a moist marine atmospheric boundary layer that is often capped by a strong inversion and stratocumulus clouds (Bretherton et al. 1995). Although specific details of individual soundings are smoothed out in the composite, the basic structure of the inversion-capped marine stratocumulus environment is evident. A dry-adiabatic marine mixed layer is shown in the lowest 200–250 m (~990 mb), with a weakly stable cumulus cloud layer from 250 to 1250 m (~895 mb), which is capped by the subsidence inversion of the anticyclone. The composite profile in Fig. 4 is unsaturated at the inversion base due to changes in the height of the inversion and stratus layers in the individual soundings contributing to the mean state. Also, the averaging probably has caused the inversion layer to have thermal and moisture gradients that are somewhat weaker than would be found in many of the individual soundings. Betts et al. (1995) analyzed the mean large-scale subsidence profile during this period (about -0.007 m s^{-1} at 1500 m AGL). This profile was superimposed on the 1D model's vertical velocities in the marine experiment to simulate the 3D processes, which helped to maintain the strength of the subsidence inversion against radiative cooling and erosion of the inversion due to entrainment from the convective PBL. Mean horizontal advection was assumed to be negligible for the composite conditions.

First in experiment 1, the 1D MM5 was initialized at 0600 UTC 11 June and was run for 72 h without the shallow-convection scheme. The model's soundings at 20 h, 40 h, and 60 h for this baseline experiment are shown in Fig. 5. Notice that almost the entire cloud layer below the inversion base becomes saturated, while maintaining a nearly dry-adiabatic thermal structure. This type of moist, unstable structure is often interpreted as a symptom of deficient performance by a convective parameterization or a resolved-scale cloud scheme (e.g., Kuo et al. 1996).

Next, the 1D MM5 was run in experiment 2 for 72 h with the shallow-convection scheme. After a few hours, the model's thermodynamic environment approaches a quasi-steady state with only a weak diurnal

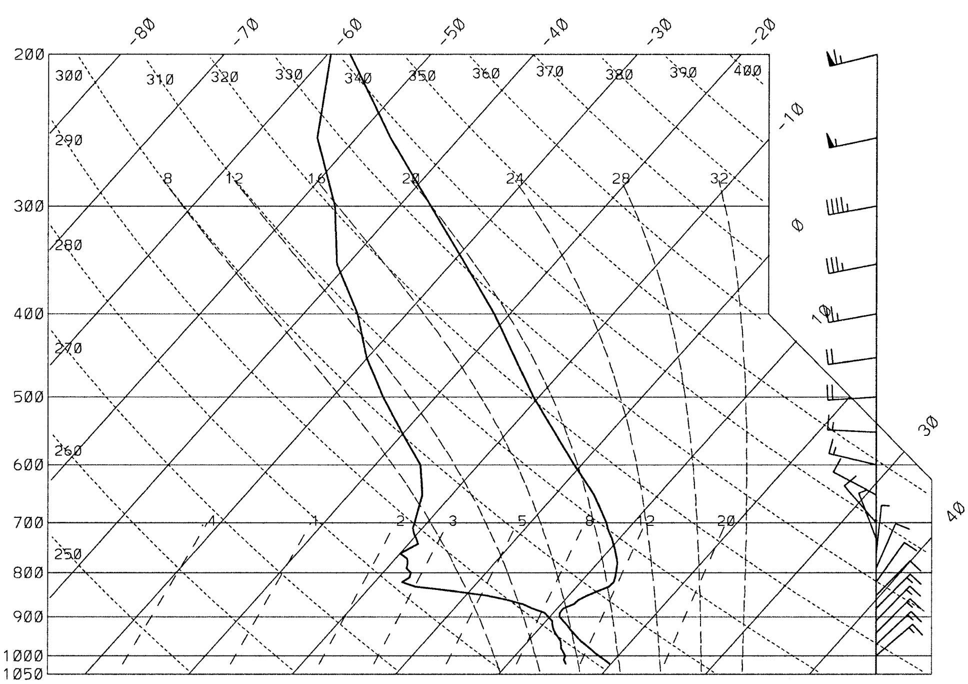

FIG. 4. Composite observed sounding calculated in the vicinity of the Azores Islands (28.00°N, 24.22°W) during ASTEX (from Betts et al. 1995).

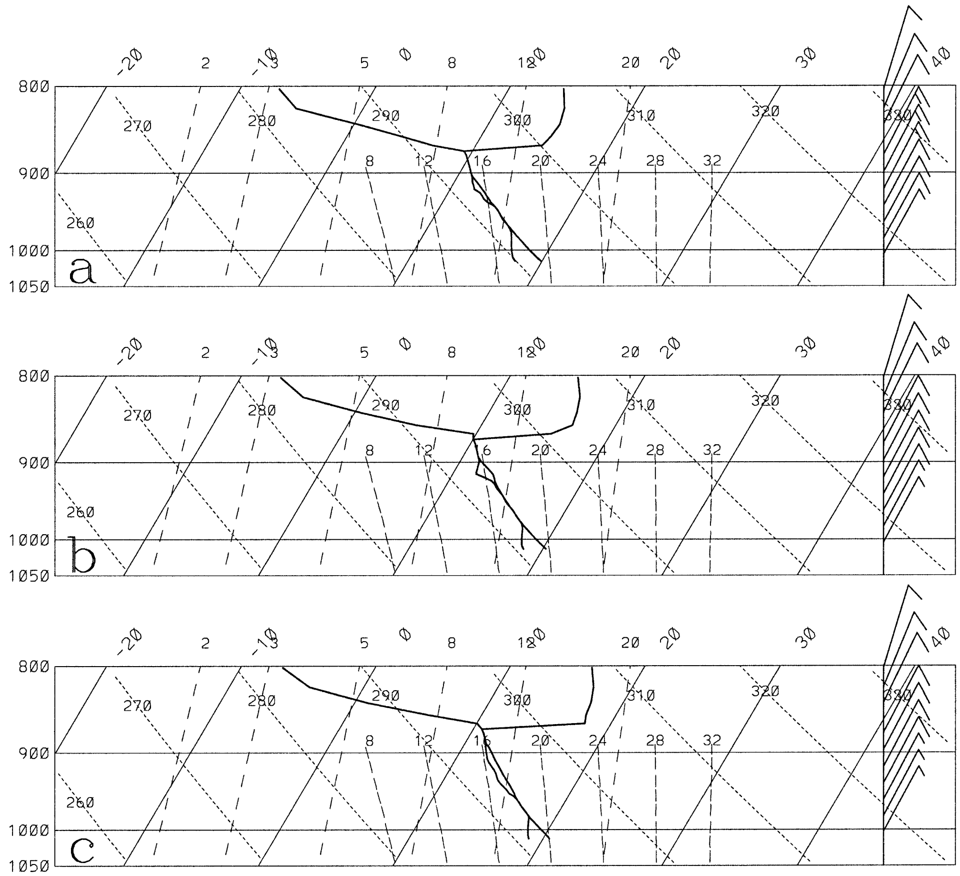

FIG. 5. Detail of model-simulated soundings without the shallow-convection scheme in expt 1 during ASTEX at 28.00°N, 24.22°W: (a) 0200 UTC 12 Jun (hour 20), (b) 2200 UTC 12 Jun (hour 40), and (c) 1800 UTC 13 Jun (hour 60).

signal below the inversion of ~0.5 C (not shown). Figure 6 shows the simulated evolution of the marine PBL height, subgrid shallow cloud base (LCL) and the top of the convective updrafts over the 72-h period. The cloud top height is steady at ~1450 m, just below the level of the inversion. Meanwhile, the PBL top ranges from about 200 to 250 m, with the LCL located slightly higher by 50–100 m, and both exhibit a weak diurnal

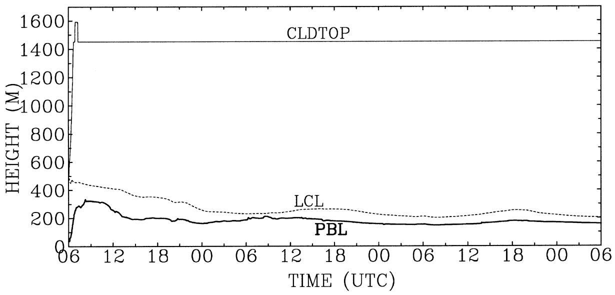

FIG. 6. Predicted cloud top (m, thin solid), planetary boundary layer (PBL) (m, heavy solid), and LCL (dotted, m) in expt 2 from 0600 UTC 11 Jun to 0600 UTC 14 Jun 1992 during ASTEX at 28.00°N, 24.22°W.

cycle due to interactions between solar and cloud processes.

Figure 7 shows that the model-simulated soundings at 20 h, 40 h, and 60 h for experiment 2 contain two distinct cloud layers. The first is a shallow (200–400 m deep) saturated stratus layer just below the inversion base at 875–895 mb. This layer is quite common in the vicinity of the Azores, but is missing from the composite, probably due to averaging over times when the layer may have been at somewhat different heights. Beneath the stratus, an unsaturated layer containing subgrid convective cloud extends from 895 to 995 mb. This cumulus layer is conditionally unstable, but not as much as in the composite sounding (Fig. 4), possibly because the model's cloud-induced mixing may be a bit too intense. The drying in the cloud layer, compared to experiment 1, is caused by convectively induced compensating subgrid subsidence. The results of experiment 2 are generally consistent with the composite profile for 11–14 June and with the mixing-line profiles of Betts and Miller (1986), but here the cloud-layer structure is formed without prescribing the thermodynamic outcome. In this weakly forced marine environment, the

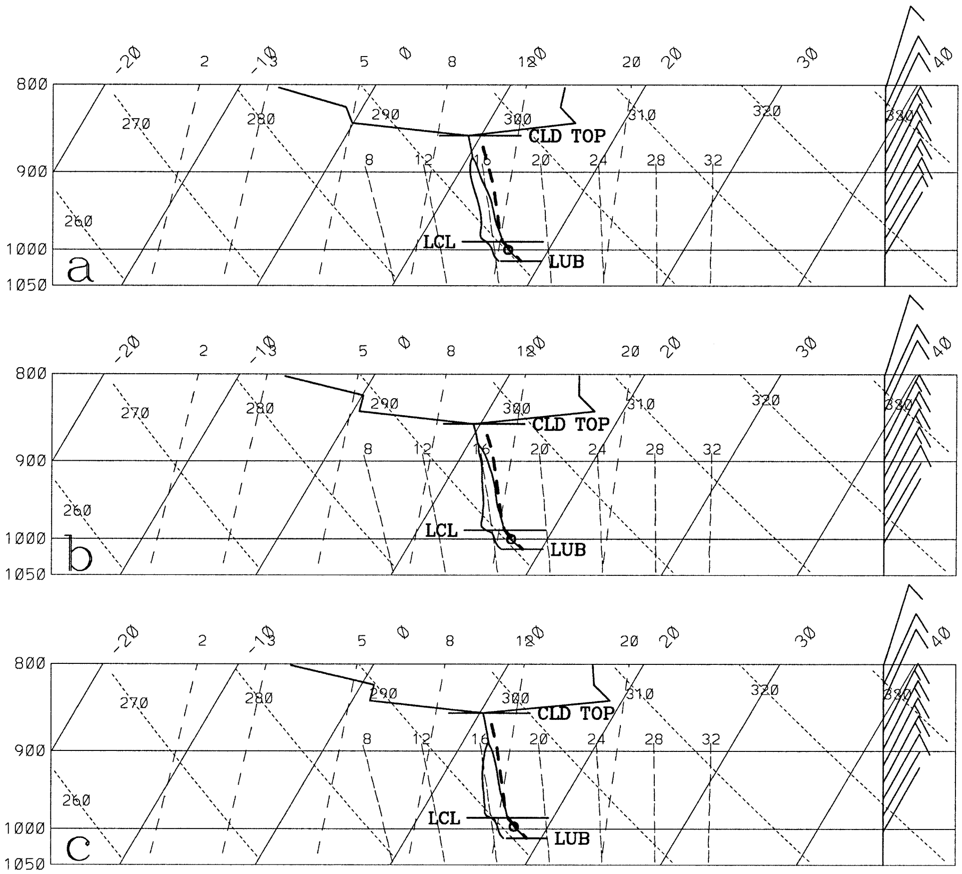

FIG. 7. Detail of model-simulated soundings with the shallow-convection scheme in expt 2 during ASTEX at 28.00°N, 24.22°W. (a) 0200 UTC 12 Jun (hour 20), (b) 2200 UTC 12 Jun (hour 40), and (c) 1800 UTC 13 Jun (hour 60). CLDTOP is the top of convective updraft and LUB is the level of the updraft base. Circle near LCL indicates the level at which parcel is released.

maximum boundary layer TKE is ~0.1 J kg^{-1} (not shown), so the vertical velocity of the cloud-initiating parcels released at the PBL top near 200 m is only ~0.3 m s^{-1}. Meanwhile, radiation flux divergence at the top of the stratus clouds and wind shear in the inversion base induce a realistic elevated turbulent layer (TKE ~ 0.3 J kg^{-1}) between 1100 and 1450 m that is completely decoupled from the PBL (not shown).

Figure 8 shows the vertical distribution of the convective and nonconvective cloud fractions and environmental relative humidity in experiment 2 at 0200 UTC 12 June 1992 (hour 20). At this time, the maximum NBC fraction is 100% just below the inversion base (darker shading represents stratus), although the convective updraft area is only about 6%. Notice that the NBC fractions are less than 10% at all levels below the stratus deck because the NBC source term, S_a, in (2.13) is small in these weakly stable layers. Rather, the convective updrafts detrain most of their mass at the stable inversion base.

Figures 9a and 9b represent time–height sections of the NBC fraction, *a,* and the grid-averaged cloud water, *l,* respectively, in experiment 2. After an initial adjustment period, both fields display primarily quasi-steady characteristics. The solid stratus deck (a = 100%) is established by ~15 h and has a depth of 200–400 m, although the cumulus updrafts are much deeper (the zero contours for a and l near 250 m approximate the convective base). As expected, the maxima in the weak diurnal cycles for these fields *in the stratus layer* occur just before sunrise. The simulated drizzle rate for the NBC (not shown) has a similar diurnal trend, with rates ranging from 0.5 to 1.5 mm day^{-1}. Most of the drizzle evaporates below the stratus base, however, where it cools and moistens the substratus layer and contributes to the diurnal trends of the LCL and PBL heights shown in Fig. 6.

Next, in Fig. 10 the relationship between cloud liquid in the updraft and in the NBC for experiment 2 is shown at 0200 UTC 12 June (hour 20), after the quasi-steady state has been attained in the model. The maximum liquid water content in the active updraft at 1450 m AGL (l_u ~ 1.6 g kg^{-1}) is considerably more than the maximum in the subgrid NBC (l_c ~ 0.55 g kg^{-1}) at about 850 m AGL. Between 1200 and 1450 m, strong detrainment at the inversion base has produced grid-

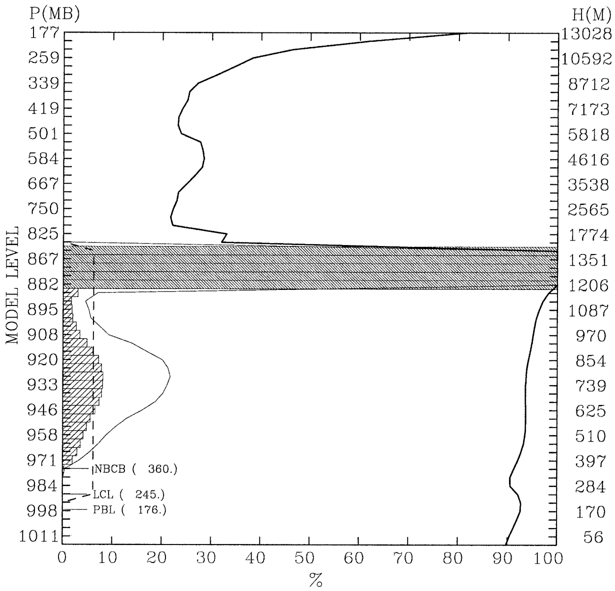

FIG. 8. Model-predicted cloud fraction (%) and resolved-scale relative humidity, RH (%), vs pressure (mb) and height (m) in expt 2 at 0200 UTC 12 Jun 1992 (hour 20) during ASTEX at 28.00°N, 24.22°W. Shading indicates NBC fraction (%), dashed line is area of shallow-cloud updraft (%), thin solid curve is effective cloud area for radiation calculations (%), and heavy curve is RH (%). NBCB is the base of NBCs.

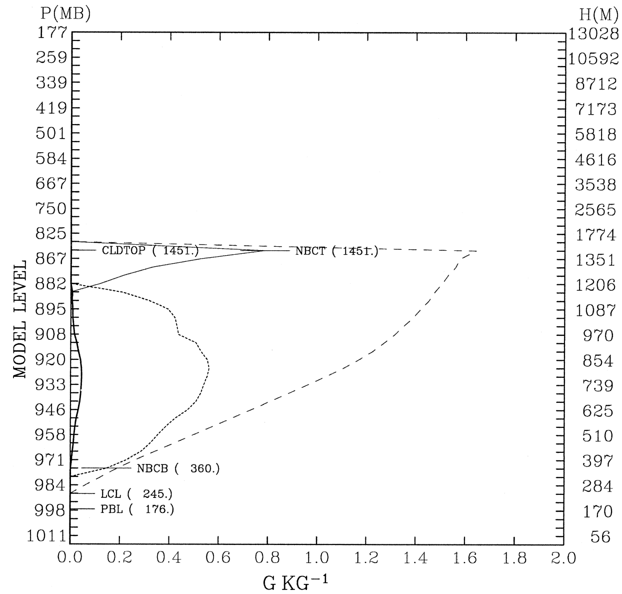

FIG. 10. Vertical profiles of predicted cloud liquid water content (LWC) (g kg^{-1}) in expt 2 at 0200 UTC 12 Jun 1992 (hour 20) during ASTEX at 28.00°N, 24.22°W. Dashed line is LWC in the updraft (l_u), dotted line is LWC in the NBC (l_c), heavy solid line is the grid-averaged LWC (l) from NBC, and thin solid line is resolved-scale LWC (q_c) when NBC area becomes 100%.

scale saturation (also see Fig. 8) so that the subgrid scale l_c is converted to grid-scale cloud water (maximum $q_c \sim 0.78$ g kg^{-1}) and l_c in these layers is set to zero. This q_c maximum at 1450 m exceeds the threshold for drizzle (0.5 g kg^{-1}), so D_{pre} contributes to explicit production of light precipitation. Moreover, the subgrid NBC liquid, l_c, near 850 m is also greater than the drizzle threshold so that $D_{\text{pre}} > 0$ at this level as well, even though grid-averaged liquid water content ($l = al_c$) is only ~0.05 g kg^{-1}.

Figure 11 demonstrates the vertical profiles of the source and sink terms, S_a and D_a, for the area of the NBC in experiment 2 in this quasi-steady marine environment at 0200 UTC 12 June 1992 (hour 20). The

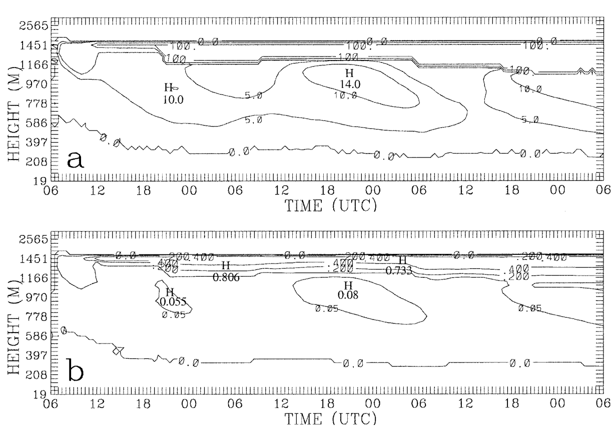

FIG. 9. Time–height section of predicted NBC in expt 2 from 0600 UTC 11 Jun to 0600 UTC 14 Jun 1992 during ASTEX at 28.00°N, 24.22°W. (a) Cloud fraction (%) and (b) horizontally averaged cloud liquid water content (g kg^{-1}). Contours for (a) are 0%, 5%, 10%, 50%, and 100%. Contours for (b) are 0.00, 0.05, 0.20, and 0.40 g kg^{-1}.

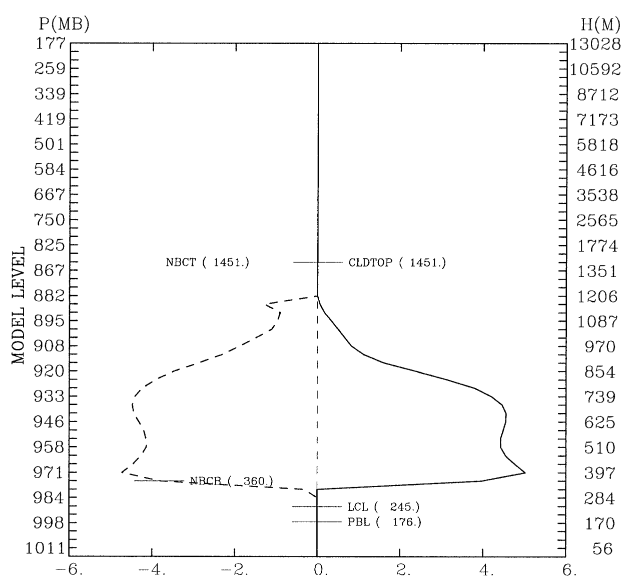

FIG. 11. Vertical profiles of the source (solid, % h^{-1}) and sink (dashed, % h^{-1}) terms in the NBC area equation (2.13) in expt 2 at 0200 UTC 12 Jun 1992 (hour 20) during ASTEX at 28.00°N, 24.22°W.

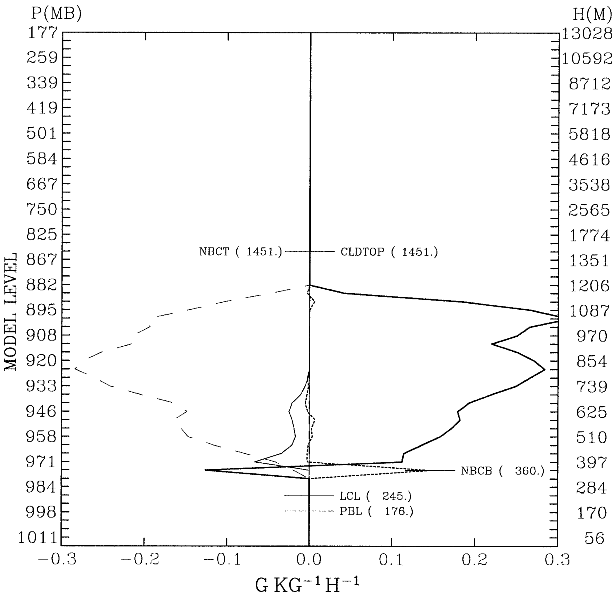

FIG. 12. Vertical profiles for the source term (heavy solid, g kg^{-1} h^{-1}) and sink terms (g kg^{-1} h^{-1}) in the NBC water-content equation (2.14) in expt 2 at 0200 UTC 12 Jun 1992 (hour 20) during ASTEX at 28.00°N, 24.22°W. Long-dashed line is depletion due to drizzle, dotted line is depletion due to in-cloud mixing, thin solid line is depletion due to mixing through exposed cloud base.

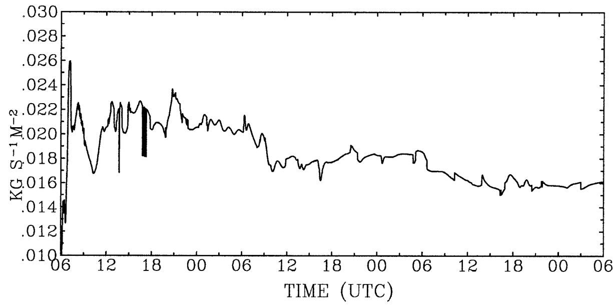

FIG. 13. Model-simulated normalized cloud-base mass flux per unit area, $\mu_B/\Delta x\Delta y$ (kg m^{-2} s^{-1}), for expt 2 from 0600 UTC 11 Jun to 0600 UTC 14 Jun 1992 during ASTEX at 28.00°N, 24.22°W.

maximum value of the source term due to updraft detrainment is ~5% h^{-1} at this time near 400 m AGL, which is approximately balanced by the sink term due to cloud-edge evaporation at ~4.8% h^{-1}. Only small departures from balanced conditions occur through the rest of the experiment. Recall that the layers near cloud top are saturated so that the convective updrafts above 1200 m detrain their mass directly onto the resolved scale, while the source term for subgrid-scale NBC becomes zero.

Next, vertical profiles for the source and sink terms of the NBC liquid water content, l_c, in (2.14) are shown for experiment 2 at 0200 UTC 12 June (Fig. 12). Maxima occur for the water source term, $S_l \sim 0.28$–0.30 g kg^{-1} h^{-1} near 895–920 mb (300–600 m below the inversion base), due to detrainment from the updraft core (1.6 g kg^{-1}, see Fig. 10) and vertical advection of cloudy air. Note that the negative source tendency near the cloud base (~360 m AGL) implies that the liquid water content in the updraft at this level is currently less than in the NBC ($l_u < l_c$). The depletion rate due to mixing through the exposed cloud bases becomes moderately negative near 970 mb, reaching about -0.07 g kg^{-1} h^{-1}, while depletion due to in-cloud mixing remains small through most cloud layers except near the cloud base. Meanwhile, drizzle clearly dominates the water depletion at this time (maximum $D_{\mathrm{pre}} \sim -0.28$ g kg^{-1} h^{-1} at 925 mb). The other sink terms are less important. The depletion due to the cloud top entrainment instability (CTEI) is not activated at this time because the instability condition is not satisfied and ice settling is inactive for this case because the cloud top is below the freezing level. As in Fig. 11, the source and sink terms for the subgrid-scale NBC become zero because the layers near cloud top are saturated so that the convective updrafts above ~1200 m detrain their mass directly onto the resolved scale.

The total cloud-base mass flux in the grid cell for the ASTEX 11–14 June episode is shown in Fig. 13. Recall that the marine PBL is quite shallow and TKE is small in this case, while the cloud updraft depth is just over 1 km. Therefore, the hybrid closure scheme is responding mostly to the TKE closure described in section 2c. The model's mass flux reveals a range lying mostly between 0.16 and 0.23 kg m^{-2} s^{-1} and a weak diurnal cycle with the flux maximums occurring near late evening times. Furthermore, vertical profiles of the shallow convection scheme's updraft mass flux, entrainment, and detrainment, using initial profiles from the Barbados Oceanographic and Meteorological Experiment in the 1D model, have been calculated with a range of values for the updraft-initiation variables to emulate a simple ensemble of cloud sizes (R. Munoz 2001, personal communication). When compared to LES-generated profiles reported by Siebesma and Cuijpers (1995), the present parameterization produced generally similar mass-flux

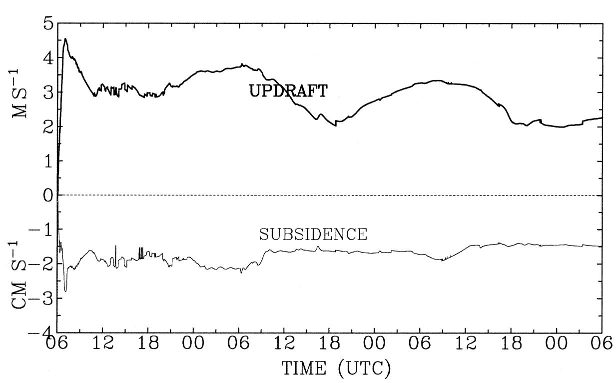

FIG. 14. Model-simulated maximums for vertical velocity in the updraft (m s^{-1}, heavy curve) and compensating subgrid-scale subsidence (cm s^{-1}, thin curve), in expt 2 from 0600 UTC 11 Jun to 0600 UTC 14 Jun 1992 during ASTEX at 28.00°N, 24.22°W.

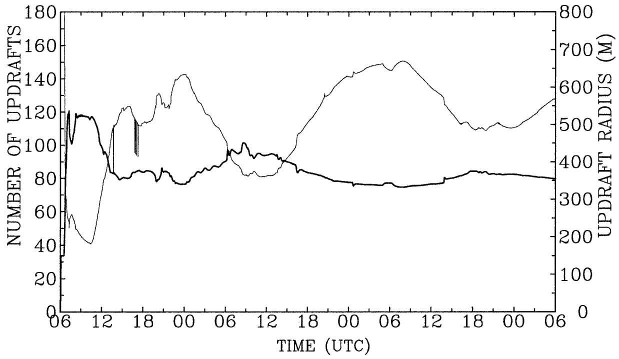

FIG. 15. Predicted updraft radius, R_c, (m, heavy curve) and number of updrafts, N_u, (thin curve) in expt 2 from 0600 UTC 11 Jun to 0600 UTC 14 Jun 1992 during ASTEX at 28.00°N, 24.22°W.

distributions. However, these preliminary experiments by Munoz also indicated that an ensemble capability could be useful for developing realistic entrainment and detrainment profiles.

Figure 14 presents the relationship between two quantities closely related to the mass flux: the maximum vertical velocity in the active convective updrafts ($W_{\max} \sim 2.0$–4.0 m s^{-1}) and the maximum compensating subsidence in the environment ($\tilde{w} \sim -1.5$ to -2.5 cm s^{-1}). The large difference in these velocities is a consequence of the comparatively small area covered by the updrafts (see Fig. 8). Finally, Fig. 15 reveals that the mean radius of the updrafts in experiment 2 is 350–500 m, while the number of updrafts in the 30 km $\times$ 30 km grid cell ranges from 40 to 150. Of course, the number of visible clouds in such an environment should be greater, because the NBCs can persist longer than the individual updrafts that generated them and we do not treat clouds with a range of sizes. Although there are inadequate data to verify many of these predictions, they demonstrate that the model can successfully maintain quasi-steady solutions and low-amplitude diurnal components that are characteristic of this weakly forced marine environment.

b. *Continental environment*

To demonstrate the response of the shallow-convection scheme in a typical continental environment, the 1D MM5 was initialized for experiment 3 with the early morning sounding from Pittsburgh, Pennsylvania, at 1200 UTC 8 June 1998 (Fig. 16) and the model was run for 24 h. The 8–9 June case began with a cool ridge of Canadian air oriented from the western Great Lakes southeastward through South Carolina. At 1200 UTC 8 June a strong storm was moving eastward from Colorado toward the Midwest. During the day on 8 June, cool northwesterly winds prevailed over western Pennsylvania beneath the midlevel subsidence inversion associated with the ridge (Fig. 16). As the storm advanced eastward early on 9 June, clouds and rain overspread the Midwest, but the prefrontal clouds did not reach Pittsburgh until about 0500 UTC. Thus, cloud generation during the daytime and evening hours was dominated by the local surface fluxes beneath the ridge and no large-scale forcing was imposed for this case. The objective of experiment 3 is to demonstrate that the shallow-convection scheme can reproduce the general

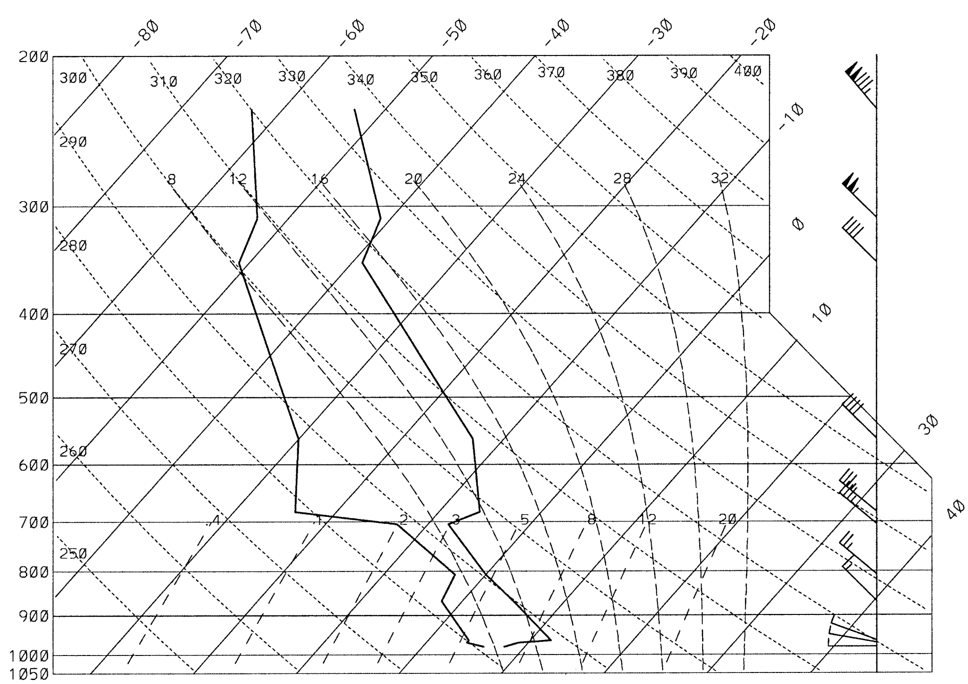

FIG. 16. Observed sounding at Pittsburgh, PA, 1200 UTC 8 Jun 1998.

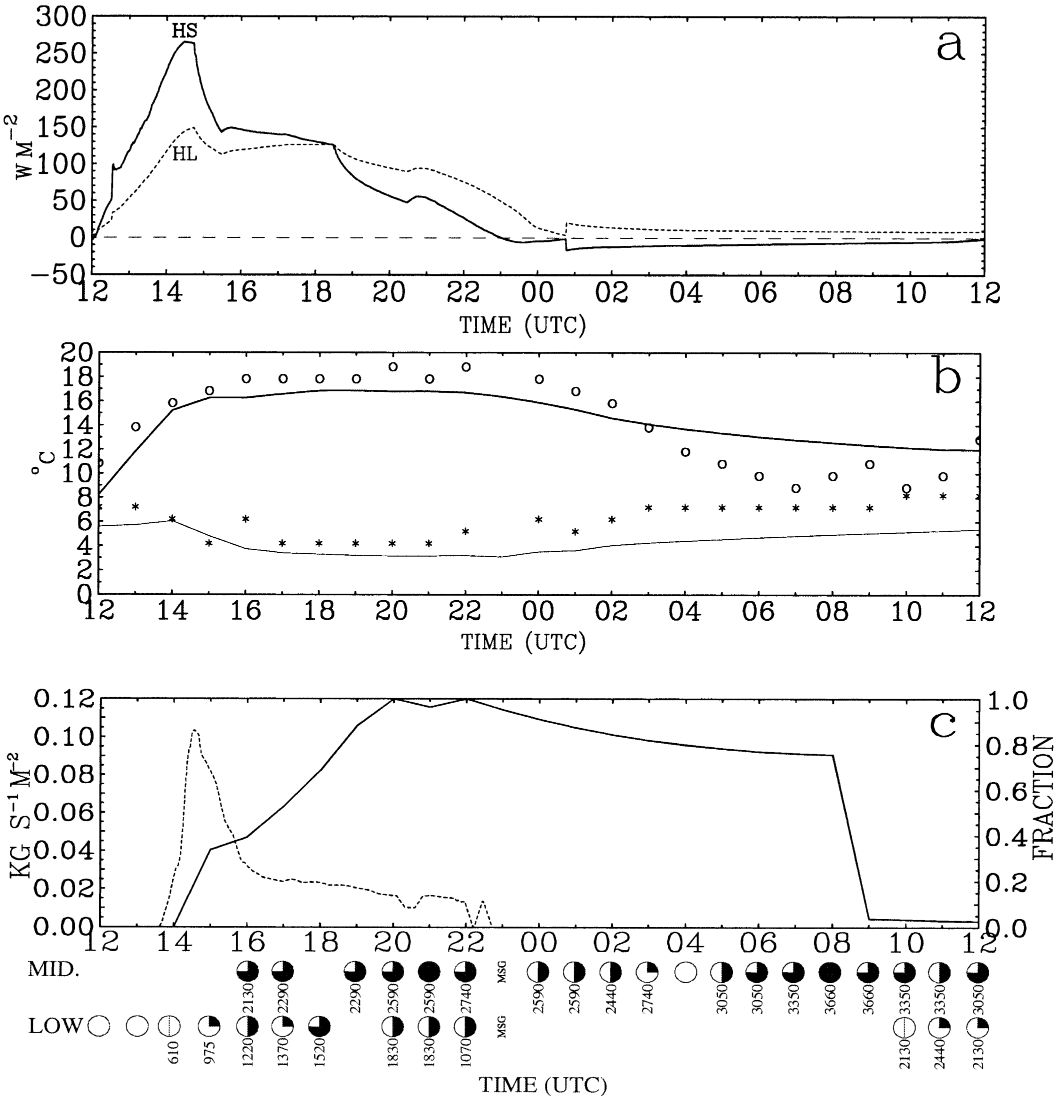

FIG. 17. Evolution of surface properties and cloud fraction at Pittsburgh in expt 3 from 1200 UTC 8 Jun to 1200 UTC 9 Jun 1998. (a) Surface sensible heat flux (solid, W m^{-2}) and latent heat flux (dotted, W m^{-2}). (b) Surface temperatures (°C), observed (circles) and simulated (heavy solid), and dewpoint temperatures (C), observed (asterisks) and simulated (thin solid). (c) Cloud fractions, observed (standard symbols) and simulated (solid), plus simulated cloud-base mass flux per unit area (dotted, kg m^{-2} s^{-1}).

characteristics of rapid cloud-fraction growth in a strongly forced daytime environment. More detailed verifications of evolving properties of the clouds themselves are presented for several land and marine cases in Part II.

Observations indicate that skies were clear in this area at 1200 UTC. The surface sensible heat flux and latent heat flux for the simulation period are shown in Fig. 17a, with the accompanying observed and simulated surface-layer temperatures and dewpoints given in Fig. 17b. These panels show strong heating in the early morning hours was abruptly curtailed just before 1500 UTC (1000 LST), after which the surface fluxes began dropping rapidly. Although there are no surface flux observations against which to compare, this scenario is confirmed by the sudden plateau reached in the surface temperature and dewpoint at 1600 UTC. Maximum temperatures observed on this June day were only 19°C.

Figure 17c displays the corresponding hourly simulated and observed cloud fractions and the modeled cloud-base mass flux at Pittsburgh. (The observed cloud fractions for the low and middle layers, shown in the circles, are given in standard NWS symbols with cloud bases shown in meters AGL.) Notice that the mass flux becomes quite large (up to 0.105 kg m^{-2} s^{-1}) during the midmorning before settling toward ~0.02 kg m^{-2} s^{-1} in the afternoon. The shallow-cloud scheme does very well at predicting the onset of shallow clouds at

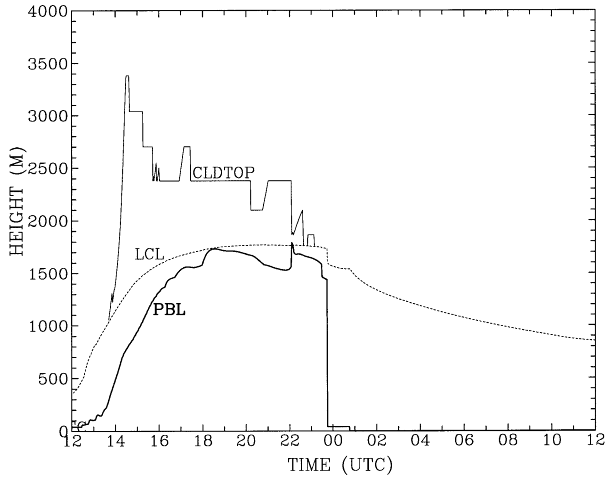

FIG. 18. Predicted cloud top (m, thin solid), planetary boundary layer (PBL) (m, heavy solid) and LCL (dotted, m) in expt 3 from 1200 UTC 8 Jun to 1200 UTC 9 Jun 1998 at Pittsburgh.

1400 UTC, followed by the rapid increase of the cloud fraction in the late morning, which coincides with the drop in simulated surface sensible heat flux. By 1700 UTC, the model simulates over 50% cloud fraction, which continues to rise to 100% by 2000 UTC (1500 LST). The simulated increase in cloud fraction is confirmed rather well by the NWS surface observations of low and midlevel clouds through this period, which verify that overcast conditions were attained by 2100 UTC.

Beginning in late afternoon, the model gradually decreases the cloud fraction, which agrees with the trend of the observations. However, the model simulates the collapse of the midlevel stratocumulus deck at 0800 UTC 9 June, whereas the observations indicate clearing occurred around 0400 UTC. Note that observations of midlevel cloud (3000–3700 m) arriving after 0500 UTC are associated with the prefrontal advection preceding the western storm as it approached the Midwest. These clouds are not of interest in experiment 3 and are not represented in the 1D model solutions.

Figure 18 shows the evolution of the PBL height, cloud base (LCL), and cloud top for the convective updrafts over the 24-h simulation. The cloud tops in the model follow a cycle that corresponds roughly to the cloud-base mass flux shown in Fig. 17c. The updrafts briefly reach 3400 m (cloud depth ~2100 m) at about 1430 UTC (0930 LST), after which they quickly settle down to about 2400 m AGL through midafternoon before gradually collapsing around sunset (about 2300 UTC). Figure 17c shows that the NBC persisted as a layer of broken stratocumulus until 0800 UTC before it finally dissipated. This agrees fairly well with the observed upper deck of broken to overcast stratocumulus reported during the day between 2200 and 2800 m. Meanwhile, the PBL top and LCL both rise rapidly through the morning and then approach 1600–1800 m in the afternoon, so the convective clouds become more shallow with time. The rise of the updraft base heights in the model is confirmed by the rise of the bases in the lower cloud layer observed at Pittsburgh (Fig. 17c). Finally, notice that Fig. 17c shows the height of the stratocumulus beneath the inversion (2200–2800 m) is distinctly lower than the layer of higher clouds (bases observed between 3000 and 3700 m) that arrived after midnight (0500 UTC). It is these higher clouds that were associated with prefrontal advection, rather than local convective processes.

The effect of the convection on the environment is shown in the model-simulated soundings at 1500 and 1800 UTC (Fig. 19). At hour 3 (1500 UTC), the PBL

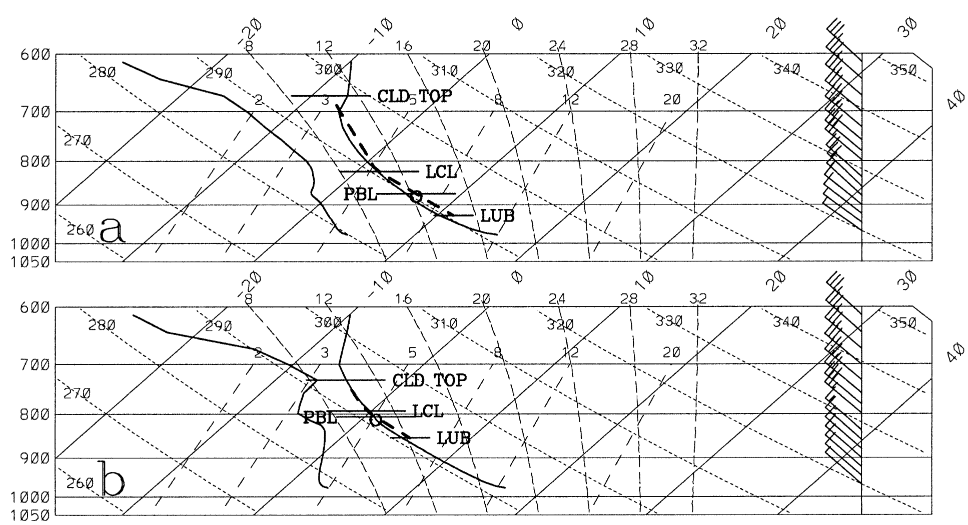

FIG. 19. Detail of model-simulated soundings with the shallow-convection scheme in expt 3 at Pittsburgh on 8 Jun 1998: (a) 1500 UTC (hour 3), (b) 1800 UTC (hour 6). CLDTOP is the top of updraft and LUB is the level of the updraft base. Circle near LCL indicates the level at which parcel is released.

top is 500 m below the LCL, but the warm, moist surface layer gives the cloud-initiating parcels sufficient buoyancy to reach the LCL, where latent heat release can help maintain buoyancy up to the inversion base near 700 mb. By hour 6 (1800 UTC), the PBL top and LCL are both near 800 mb and the cloud top has lowered a bit to 730 mb (2700 m AGL). Notice that the unsaturated cloud layer is nearly moist adiabatic at 1800 UTC due to the cloud-induced mixing in the layer. Also, Fig. 19 reveals that the cloud-updraft temperature is only slightly warmer than its environment at 1800 UTC and is generally less buoyant than at 1500 UTC, so the vertical moisture flux weakens with time. This contributes to allowing the layer beneath the inversion to remain unsaturated until midafternoon.

Figure 20 shows the vertical distribution of convective and neutrally buoyant cloud fraction and environmental relative humidity at 1500 UTC (cf. Fig. 19a). At this time, the maximum NBC fraction is already about 34% near 3000 m and decreases downward, while the convective updraft area covers only about 7% of the area. Consistent with the sounding of Fig. 19a, the environment is rather dry at 1500 UTC with a maximum relative humidity of about 70% near 1700 m AGL. The thin solid curve in Fig. 20 shows that the maximum ''effective'' cloud fraction used in the calculation of the radiation fluxes is about 65% in a thin ''anvil-like'' layer (see section 3). The vertical profiles of cloud water at hour 3 (not shown) indicate that the maximum liquid water content in the active updraft (l_u) is about 2.1 g kg^{-1}, which is considerably larger than that in the subgrid NBC (l_c, about 1.0 g kg^{-1}). However, since $l_c >$ 0.5 g kg^{-1} (the drizzle threshold), the precipitation mechanism becomes an effective process for depleting cloud water from the NBC, even though the maximum resolved-scale cloud water, $l = al_c$, is only 0.34 g kg^{-1} at this time. None of this drizzle reaches the ground because of the low relative humidity below cloud base. Figure 21 shows that the source and sink terms for the NBC area, S_a and D_a, are strongly unbalanced during the midmorning heating cycle (1500 UTC), so the cloud area is growing rapidly at a rate of 30% h^{-1}. This time corresponds to the period of rapid cloud-area expansion shown in Fig. 17c.

Further examination of the results indicated that the simulated clouds first formed in experiment 3 at 1345 UTC with bases near 1000 m AGL, radii of 150 m, and about 290 clouds in the 30-km grid cell (not shown). Since the cloud tops grew rapidly to the inversion level during the next hour, the radius also grew to ~1300 m and the number of active updrafts necessary to provide sufficient cloud base mass flux dropped to about 10. The vertical velocity in the convective updrafts was generally 2–3 m s^{-1} through most of the day, although it briefly grew to ~8.5 m s^{-1} at 1430 UTC when the convection was deepest and first reached the inversion layer (the time of largest cloud-base mass flux). As in experiment 2 (Fig. 14), the compensating sinking motion was about two orders of magnitude less than the updraft maximum. Most of the other cloud characteristics simulated by the 1D model in experiment 3 were similar to those found in the marine case of episode 2.

Qualitatively, the shallow-cloud simulations in this case appear to be fairly representative of many evolving continental convective environments. That is, convection commonly begins as many small cumuli in the midmorning, but these become fewer and larger with time as the cloud depth increases. Of course, these qualitative assessments and limited verifications against data can serve only as an initial representation of the general characteristics of the shallow-convection scheme. A more through quantitative evaluation in a variety of well-observed cloud environments, including 3D applications, is necessary to determine the suitability of the parameterization for more general use.

5. Summary

A shallow-convection parameterization designed to represent both marine and continental environments has been developed for use in mesoscale models. The scheme is consistent with the explicit moisture, deep convection, radiation, and turbulence physics of the MM5 model. In particular, it transitions to the Kain–Fritsch deep-convection scheme when simulated cloud depths exceed a critical depth, D_{KF}, or to the Dudhia explicit-moisture scheme when shallow clouds spread to saturate a grid element in a more stable environment.

The parameterized shallow convection is triggered primarily by boundary layer turbulence processes via the model-predicted TKE. Cloud depth is calculated using parcel buoyancy theory, but the cloud top grows gradually as a function of the updraft velocity maximum, rather than instantaneously as in the Kain–Fritsch scheme. The closure for the cloud-base mass flux is based on a hybrid formulation that combines a CAPE-removal closure for deeper clouds (as in the KF deep convection) and a TKE-based closure for very shallow clouds. This flexible hybrid assumption has been tested in case studies over land and oceans and has been found to perform reasonably well in all cases (also see Part II).

Cloudy air in the convective updrafts is detrained from the 1D cloud model into a class of approximately neutrally buoyant clouds, or NBCs. Prognostic equations are used to predict the NBC fraction and liquid/ice content. The NBCs can dissipate through several physical processes, including evaporation at cloud edge due to horizontal turbulent mixing, vertical diffusion, precipitation, ice settling, and cloud-top entrainment instability (CTEI).

Using a 1D version of the PSU–NCAR MM5, the shallow-convection parameterization was demonstrated in two preliminary experiments for marine and continental environments. The simulations produced qualitatively realistic thermodynamic structures and cloud

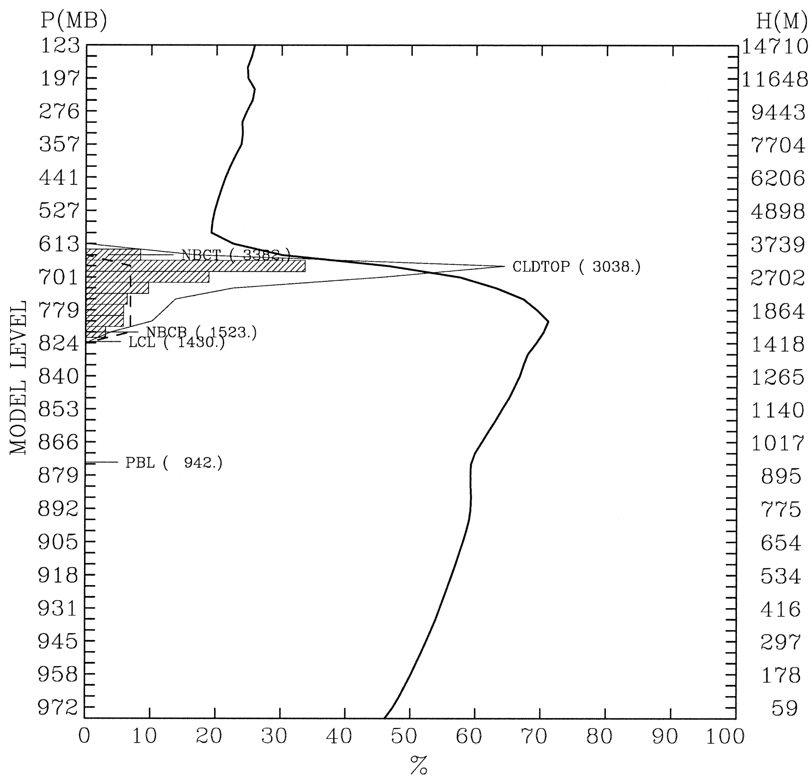

FIG. 20. Model-predicted cloud fraction (%) and resolved-scale relative humidity, RH (%), vs pressure (mb) and height (m) in expt 3 at 1500 UTC 8 Jun 1998 (hour 3) at Pittsburgh. Shading indicates NBC fraction (%), dashed line is area of shallow-cloud updraft (%), thin solid curve is effective cloud area for radiation calculations (%), and heavy curve is RH (%). NBCB and NBCT are the base and top of NBCs, respectively.

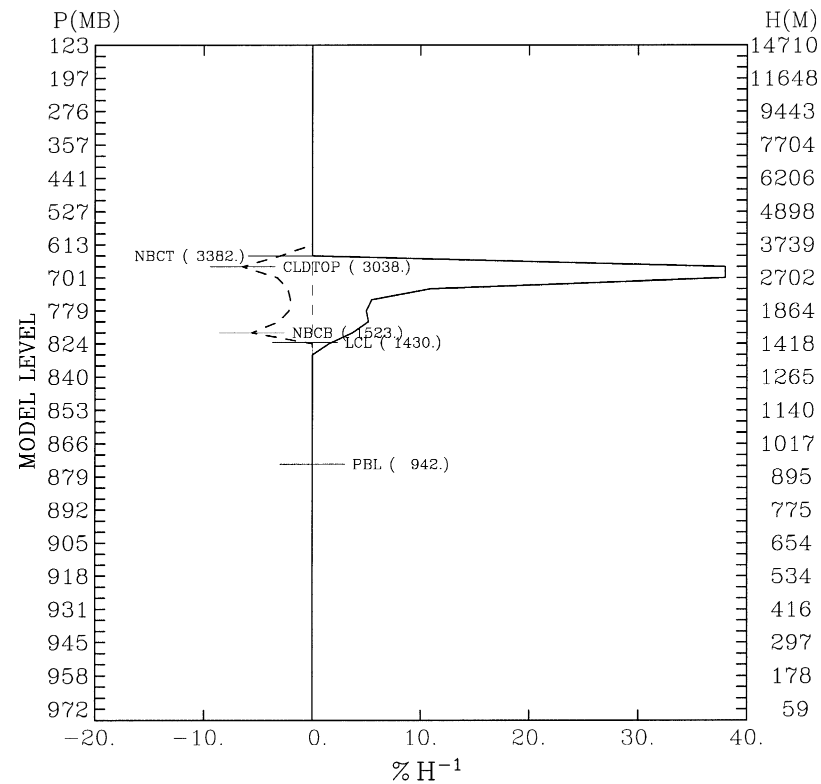

FIG. 21. Vertical profiles of the source (solid, % h^{-1}) and sink (dashed, % h^{-1}) terms in the NBC area equation (2.13) in expt 3 at 1500 UTC, 8 Jun 1998 (hour 3) at Pittsburgh.

fields in both cases. The weakly forced 3-day marine case, initialized with an ASTEX composite sounding, produced a quasi-steady solution with 6%–13% cumulus-cloud areas topped by a stratus deck beneath the inversion of the Bermuda high. The subgrid scale shallow convection was shown to be important for preventing overmoistening of the CTBL by forcing compensating subsidence in the cloud environment.

For the more strongly forced continental case, initially clear skies in the vicinity of Pittsburgh, Pennsylvania, developed many small shallow cumuli before midmorning, which rapidly grew until reaching an inversion base near 700 mb. Capped by the midtropospheric inversion, updraft detrainment soon led to a stratocumulus layer that eventually covered 90%–100% of the sky by midafternoon, matching observed cloud-area growth quite well. Meanwhile, simulated cloud bases rose during the morning in response to the growth of the turbulent boundary layer, gradually causing cloud depths to decrease. In contrast to the marine case, the continental case displayed strong forcing and rapid changes in cloud characteristics, demonstrating the versatility of the scheme. The next step is to perform more detailed evaluations in both types of environments for cases having cloud-specific observations, for which the reader is directed to Part II of this paper. This will be followed by regional applications in the 3D MM5 model.

Acknowledgments. This research has been supported by the U.S. Environmental Protection Agency through Grant No. R825254-01-0 and by the National Aeronautical and Space Administration through Grant No. NAG8-1530.

REFERENCES

Ackerman, T. P., 1991: A tutorial on global atmospheric energetics and the greenhouse effect. *Global Warming: Physics and Facts,* B. G. Levi, D. Hafemeister, and R. Scribner, Eds., American Institute of Physics, 1–23.

Agee, E. M., 1987: Mesoscale cellular convection over the oceans. *Dyn. Atmos. Oceans,* **10,** 317–341.

Albrecht, B. A., 1979: A model of the thermodynamic structure of the trade-wind boundary layer. Part II: Applications. *J. Atmos. Sci.,* **36,** 90–98.

——, 1993: Effects of precipitation on the thermodynamic structure of the trade-wind boundary layer. *J. Geophys. Res.,* **98,** 7323–7337.

——, C. S. Bretherton, and D. Johnson, 1995: The Atlantic Stratocumulus Transition Experiment (ASTEX). *Bull. Amer. Meteor. Soc.,* **76,** 889–904.

——, A. K. Betts, W. H. Schubert, and S. K. Cox, 1979: A model of the thermodynamic structure of the trade-wind boundary layer. Part I: Theoretical development and sensitivity tests. *J. Atmos. Sci.,* **36,** 73–89.

Arakawa, A., and W. H. Schubert, 1974: Interaction of a cumulus cloud ensemble with the large-scale environment, Part I. *J. Atmos. Sci.,* **31,** 674–701.

Betts, A. K., 1973: Non-precipitating cumulus convection and its parameterization. *Quart. J. Roy. Meteor. Soc.,* **99,** 178–196.

——, 1986: A new convective adjustment scheme. Part I: Observational and theoretical basis. *Quart. J. Roy. Meteor. Soc.,* **112,** 677–692.

——, and M. Miller, 1986: A new convective adjustment scheme. Part II: Single column tests using GATE wave, BOMEX, ATEX and arctic air-mass data sets. *Quart. J. Roy. Meteor. Soc.,* **112,** 693–709.

——, and R. Bores, 1990: A cloudiness transition in a marine boundary layer. *J. Atmos. Sci.,* **47,** 1480–1497.

——, C. S. Bretherton, and E. Klinker, 1995: Relation between mean boundary-layer structure and cloudiness at the R/V *Valdivia* during ASTEX. *J. Atmos. Sci.,* **52,** 2752–2762.

Black, T. L., 1994: The new NMC mesoscale eta model: Description and forecast examples. *Wea. Forecasting,* **9,** 265–278.

Bretherton, C. S., E. Klinker, A. K. Betts, and J. A. Coakley, 1995: Comparison of ceilometer, satellite, and synoptic measurements of boundary layer cloudiness and the ECMWF diagnostic cloud parameterization scheme during ASTEX. *J. Atmos. Sci.,* **52,** 2736–2751.

Chappell, C. F., E. L. Magaziner, and J. M. Fritsch, 1974: On the computation of isobaric wetbulb temperature and saturation temperature over ice. *J. Appl. Meteor.,* **13,** 726–728.

Cuijpers, J. W. M., and P. G. Duynkerke, 1995: Large eddy simulation of trade-wind cumulus clouds. *J. Atmos. Sci.,* **52,** 650–666.

Deardorff, J. W., 1980: Cloud top entrainment instability. *J. Atmos. Sci.,* **37,** 131–146.

Del Genio, A. D., M.-S. Yao, W. Kovari, and K. K.-W. Lo, 1996: A prognostic cloud water parameterization for global climate models. *J. Climate,* **9,** 270–304.

Deng, A., 1999: A shallow convection parameterization scheme for mesoscale models. Ph.D. thesis, The Pennsylvania State University, 152 pp.

——, N. L. Seaman, and J. S. Kain, 2003: A shallow-convection parameterization for mesoscale models. Part II: Verification and sensitivity studies. *J. Atmos. Sci.,* **60,** 57–78.

Dudhia, J., 1989: Numerical study of convection observed during the winter monsoon experiment using a mesoscale two-dimensional model. *J. Atmos. Sci.,* **46,** 3077–3107.

Fritsch, J. M., and C. F. Chappell, 1980: Numerical prediction of convectively driven mesoscale pressure system. Part I: Convective parameterization. *J. Atmos. Sci.,* **37,** 1722–1733.

Gayno, G. A., 1994: Development of a higher-order, fog-producing boundary layer model suitable for use in numerical weather prediction. M.S. thesis, Department of Meteorology, The Pennsylvania State University, 104 pp.

Grant, A. L. M., and A. R. Brown, 1999: A similarity hypothesis for shallow-cumulus transports. *Quart. J. Roy. Meteor. Soc.,* **125,** 1913–1936.

Gregory, D., 2001: Estimation of entrainment rate in simple models of convective clouds. *Quart. J. Roy. Meteor. Soc.,* **127,** 53–72.

——, and P. R. Rowntree, 1990: A mass flux convection scheme with representation of cloud ensemble characteristics and stability-dependent closure. *Mon. Wea. Rev.,* **118,** 1483–1506.

Grell, G. A., J. Dudhia, and D. R. Stauffer, 1994: A description of the fifth generation Penn State/NCAR Mesoscale Model (MM5). NCAR Tech. Note NCAR TN-398-STR, 138 pp.

Kain, J. S., and J. M. Fritsch, 1990: A one-dimensional entraining/detraining plume model and its application in convective parameterization. *J. Atmos. Sci.,* **47,** 2784–2802.

——, and J. M. Fritsch, 1993: Convective parameterization in mesoscale models: The Kain–Fritsch scheme. *The Representation of Cumulus Convection in Numerical Models, Meteor. Monogr.,* No. 46, Amer. Meteor. Soc., 165–170.

Kreitzberg, C. W., and D. J. Perkey, 1976: Release of potential instability. Part I: A sequential plume model within a hydrostatic primitive equation model. *J. Atmos. Sci.,* **33,** 456–475.

Kuo, Y.-H., R. J. Reed, and Y. Liu, 1996: The ERICA IOP5 storm: Mesoscale cyclogenesis and precipitation parameterization. *Mon. Wea. Rev.,* **124,** 1409–1434.

Lamb, R. G., 1982: Diffusion in the convective boundary layer. *At-*

mospheric Turbulence and Air Pollution Modelling, F. T. M. Nieuwstadt and H. van Dop, Eds., Reidel, 159–229.

Lilly, D. K., 1968: Models of cloud-topped mixed layers under a strong inversion. *Quart. J. Roy. Meteor. Soc.,* **94,** 292–309.

MacVean, M. K., and P. J. Mason, 1990: Cloud-top entrainment instability through small-scale mixing and its parameterization in numerical models. *J. Atmos. Sci.,* **47,** 1012–1030.

McHenry, J. N., J. S. Kain, and J. E. Pleim, 1996: Development and testing of a Kain–Fritsch-based deep convective cloud chemistry scheme for incorporation into multiscale air quality models. Preprint, *Ninth Joint Conf. on Applications of Air Pollution Meteorology with A&WMA,* Atlanta, GA, Amer. Meteor. Soc., 207–212.

Randall, D. A., 1980: Conditional instability of the first kind upside-down. *J. Atmos. Sci.,* **37,** 125–130.

Rao, G., 1996: Large eddy simulation of turbulent flow in a marine convective boundary layer with snow. *J. Atmos. Sci.,* **53,** 86–100.

Schlesinger, R. E., 1984: Effects of the pressure perturbation field in numerical model of unidirectionally sheared thunderstorm convection: Two versus three dimensions. *J. Atmos. Sci.,* **41,** 1571–1587.

Shafran, P. C., N. L. Seaman, and G. A. Gayno, 2000: Evaluation of numerical predictions of boundary-layer structure during the Lake Michigan Ozone Study (LMOS). *J. Appl. Meteor.,* **39,** 412–426.

Siebesma, A. P., 1997: The impact of mesoscale convective-system potential vorticity anomalies on numerical-weather-prediction forecasts. *Quart. J. Roy. Meteor. Soc.,* **123,** 73–88.

——, and J. W. M. Cuijpers 1995: Evaluation of parametric assumptions for shallow cumulus. *J. Atmos. Sci.,* **52,** 650–666.

——, and A. A. M. Holtslag, 1996: Model impacts of entrainment and detrainment rates in shallow cumulus convection. *J. Atmos. Sci.,* **53,** 2354–2364.

Simpson, J., 1983: Cumulus clouds: Interactions between laboratory experiments and observations as foundations for models. *Mesoscale Meteorology,* D. K. Lilly and T. GalChen, Eds., Reidel, 399–412.

——, and V. Wiggert, 1969: Models of precipitating cumulus towers. *Mon. Wea. Rev.,* **97,** 471–489.

Stull, R. B., 1988: *An Introduction to Boundary Layer Meteorology.* Kluwer Academic, 666 pp.

Tiedtke, M., 1989: A comprehensive mass flux scheme of cumulus parameterization in large-scale models. *Mon. Wea. Rev.,* **117,** 1779–1800.

——, 1993: Representation of clouds in large-scale models. *Mon. Wea. Rev.,* **121,** 3040–3060.

Wang, S., 1993: Modeling marine boundary-layer clouds with a two-layer model: A one-dimensional simulation. *J. Atmos. Sci.,* **50,** 4001–4021.

Weil, J. C., 1988: Dispersion in the convective boundary layer. *Lectures on Air Pollution Modeling,* A. Venkatram and J. C. Wyngaard, Eds., Amer. Meteor. Soc., 167–227.

Wetzel, P. J., S. Argentini, and A. Boone, 1996: The role of the land surface in controlling daytime cloud amount: Two case studies in the GCIP-SW area. *J. Geophys. Res.,* **101D,** 7359–7370.

Wyant, M. C., C. S. Bretherton, H. A. Rand, and D. E. Stevens, 1997: Numerical simulations and a conceptual model of the Stratocumulus to trade cumulus transition. *J. Atmos. Sci.,* **54,** 168–192.

Xu, K., and D. A. Randall, 1996: A semiempirical cloudiness parameterization for use in climate models. *J. Atmos. Sci.,* **53,** 3048–3102.

Young, G. S., 1987: Mixed layer spectra from aircraft measurements. *J. Atmos. Sci.,* **44,** 1251–1256.